12-2011

Design and Implementation of Metamaterial Based Strain Sensor Using Aperture Coupled Antenna

Michael Brandon Buscher
University of Arkansas

Recommended Citation
Buscher, Michael Brandon, "Design and Implementation of Metamaterial Based Strain Sensor Using Aperture Coupled Antenna" (2011). *Theses and Dissertations*. 187.
http://scholarworks.uark.edu/etd/187

DESIGN AND IMPLEMENTATION OF METAMATERIAL BASED STRAIN SENSOR USING APERTURE COUPLED ANTENNA

DESIGN AND IMPLEMENTATION OF METAMATERIAL BASED STRAIN SENSOR USING APERTURE COUPLED ANTENNA

A thesis submitted in partial fulfillment
of the requirements for the degree of
Master of Science in Electrical Engineering

By

Michael Brandon Buscher
University of Arkansas
Bachelor of Science in Electrical Engineering, 2009
University of Arkansas
Bachelor of Arts in Physics, 2009

December 2011
University of Arkansas

ABSTRACT

Strain sensors are used to convert the physical measured quantity of strain into an electrical signal suitable for processing by electronic equipment. Traditional strain sensors are comprised of a thin flexible film with a resistive pattern traced on the surface. As the sensor is deformed, the electrical resistance changes proportionally, giving a direct measure of the strain incurred. Metamaterials, particularly split ring resonators (SRR), lend themselves as a valuable tool for sensing applications due to their highly resonant nature and their very narrow bandwidth (high Q-factor). Due to very high field localization effects, they are extremely sensitive to both the dielectric properties of the materials they are deposited on and in close proximity to, allowing for a high degree of tunability. The benefit of using metamaterials as a sensor lies in the fact that as a microwave device, they can be used to realize passive wireless sensors as compared to the current technology which requires supporting circuitry to measure and transmit data. This thesis will address the feasibility of implementing a metamaterial based strain sensor that exploits the tunable nature of the SRR as it is calibrated with a traditional resistive strain sensor and then applied to quantify the strain incurred on a loaded cantilever beam.

This thesis is approved for
recommendation to the
Graduate Council

Thesis Director:

Dr. Vasundara V. Varadan

Thesis Committee:

Dr. Reeta Vyas

Dr. Jinxian Wu

THESIS DUPLICATION RELEASE

I hereby release the University of Arkansas Libraries to duplicate this thesis when needed for research and scholarship.

Agreed ____

Michael Brandon Buscher

Refused ____

Michael Brandon Buscher

ACKNOWLEDGEMENTS

I would like to acknowledge Dr. Vasundara Varadan for her guidance and support throughout my college education. I would also like to thank my current and former lab-mates: Dr. In Kwang Kim, Mr. Liming Ji, and Mr. Atanu Dutta for their invaluable help and advice with both research and academic study.

DEDICATION

This Masters Degree work is dedicated to my fiancée Mikaela, my parents Mike and Terri, and my brother Nathan, who have offered never-ending support throughout my entire collegiate career.

TABLE OF CONTENTS

LIST OF TABLES

LIST OF FIGURES

I. INTRODUCTION

This thesis will discuss the design and implementation of an effective metamaterial based strain sensor. As technology continues to advance, the level of automation and sophistication of everyday devices continues to increase. Nearly all electrical or electronic devices require conversion of some physical stimulus into an electrical signal through a sensor. Sensors are increasingly prevalent and the desire for low cost wireless sensors is ever present.

One area of great interest for sensor applications is structural analysis. Nearly all mechanical structures are subject to a great deal of design and simulation prior to actual fabrication. After these structures are fabricated, there are many instances where knowledge of the current status of the system is desirable. Structures such as bridges and high-rise buildings are always exposed to stresses from the outside world. Strain sensors allow for active measurement of the mechanical strain a structure experiences, leading to insights about the material being measured. This information can be used to determine if a structure is overloaded, fatiguing, or about to fail; providing invaluable diagnostic information which will aid in deploying maintenance as well as gathering information for future designs.

Typically, strain gauges are wired devices which use DC or relatively low frequency AC signals for measurement. There are, however, many instances where a traditional strain gauge is not practical. An example of such a situation would be the measurement of strain induced in a helicopter rotor blade. The helicopter blade is a perfect example of a beam.

Figure 1 – A helicopter in flight prepares to lift another helicopter after being stranded. The rotor blades of the helicopter are deformed by extremely large amounts. These blades are acting as loaded cantilever beams with the anchor point at the hub of the rotor.

The blade is fixed at the rotor hub, and depending on the size of the helicopter, the free end of the rotor blade may be deflected by distances on the order of meters. While measuring the strain at several points on the rotor blade would be useful, there are several obstacles which would make measurement difficult, if not impossible.

The most prominent difficulty in this scenario with retrieving the measurement data using current technology is the necessity of a wired connection between the sensor and the measurement equipment. Desire for the measurement of systems such as the helicopter rotor, where there is no simple option for placing and communicating with traditional wired sensing devices gives motivation for the design of wireless sensing mechanisms.

The primary components in any sensor application are the measurement equipment, the sensor, and any data processing backend. Ideally, a wireless sensor would be a passive device, requiring no power source for the transmission of the measurement back to the measurement equipment. This criterion hints at the need for a device whose sensing mechanism is based in microwave engineering, where the property being measured will alter the microwave properties of the sensor itself in a linear manner, to match the stress-strain relationship of a cantilever beam [1], without any need for signal conversion. It is the goal of this thesis to present a sensor topology which provides a proof of concept for a reasonable use of metamaterials, particularly split ring resonators (*SRR's*) as a sensing medium for strain, with the ability to be extended to any area where capacitive sensors are applicable, such as fluid fill level or pressure quantification.

1.1 Beam Mechanics

A beam is a body whose cross-section is small in comparison to its length. Beams are generally categorized based on their geometry, the manner in which they are supported and the type of loading. Geometrical classifications are typically based on the cross-sectional shape, the profile of the beam, and the presence of any taper in the beam being described. Common types of support for beams are shown below, in Figure 2. Loading categorizations include beams with distributed loads of a given profile and loads at given points along the length of the beam. This thesis will be referring to the case of the end loaded cantilever beam for all experimental work.

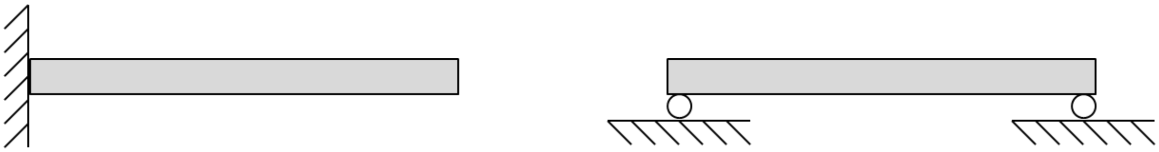

(a) Cantilever Beam

(b) Simply Supported Beam

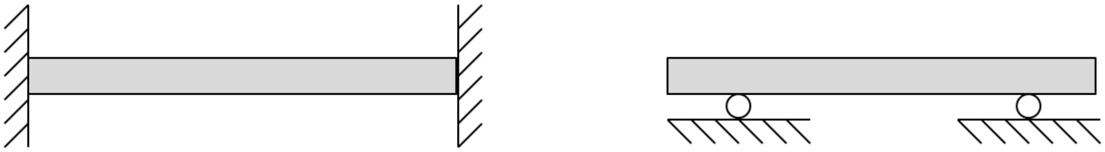

(c) Fixed Ended Beam

(d) Overhanging Beam

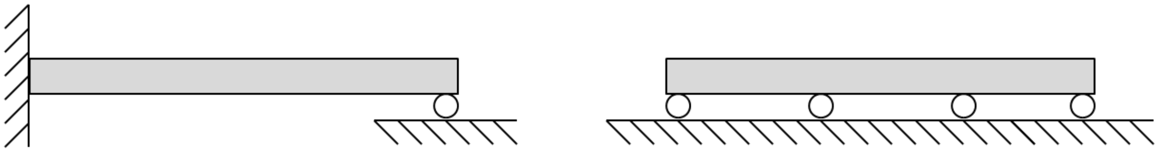

(e) Simply Supported Cantilever Beam

(f) Continuously Supported Beam

Figure 2 – Several common examples of beam supporting scenarios. This thesis deals with the case of the cantilever beam (a). A load will be applied to the end of the beam in order to cause a deformation or bending of the beam and electrical sensors will be placed to quantify the effect.

An end-loaded cantilever beam is a beam rigidly supported at one end while the other end is left free to support a load. The force of the load is transverse to the beam, lacking twisting or axial effects, and carried by the beam to the supporting structure. This is a fundamental building block in mechanical systems. The cantilever beam problem is described by the physical parameters of the structure: length, width, and thickness. The beam is also described by the Young's modulus, or the modulus of elasticity from Hooke's Law which is used to relate the beam stress to the applied strain. In the mechanical engineering representation of Hooke's law, stress is typically denoted as σ, and strain is denoted as ε. This will likely cause confusion as these symbols are known in electrical engineering to represent conductivity and electric permittivity of a material. For this reason, any reference to stress shall be noted as "σ_{mech}," and any reference to strain shall be denoted as ε_{mech}.

$$\sigma_{mech} = E\epsilon_{mech} \tag{1}$$

The mechanics problem in question is detailed below. A cantilever beam is loaded at its free endpoint by an object of mass M. With the physical properties of the beam known (length, width, thickness) and the Young's modulus of the beam material known, the deflection of the beam may be calculated.

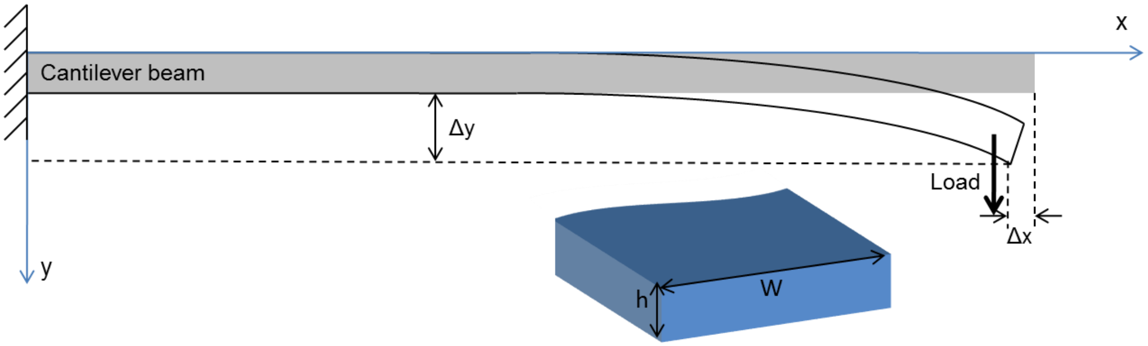

Figure 3 – General view of the mechanics problem for the end loaded cantilever beam. The quantities of interest are the physical dimensions of the beam and the Young's modulus of the material. From these known quantities the deflection of the beam can be computed.

Bending of a beam due to normal bending stress is typically described using the Euler-Bernoulli beam equation. In order to satisfy the Euler-Bernoulli equation below, in equation (2), several constraints must be met:

1. The beam is subject only to pure bending; that is, no shear force, and no torsion or axial loading is present.
2. The material is isotropic and homogeneous.
3. The material obeys Hooke's law.
4. The beam is initially straight with constant cross-section.

5. The beam has an axis of symmetry in the plane of bending.
6. The proportions of the beam are such that the beam would fail from bending instead of crushing, wrinkling, or buckling.
7. The cross section of the beam remains planar during bending.

The beam will experience both shear and tensile/compressive forces from the load. The compressive forces experienced by the beam are highest on the side of the beam in the direction of the loading force, while the tensile forces are highest on the opposite side of the beam. Both of these forces induce stress in the beam. As there are two opposing forces on opposing surfaces of the beam, it is implied that there is a point between the two surfaces where no stress is incurred; this is referred to as the *neutral plane*. The bending stress varies linearly from the neutral axis [1].

$$\frac{d^2}{dx^2}\left(EI\frac{d^2w}{dx^2}\right) = q \tag{2}$$

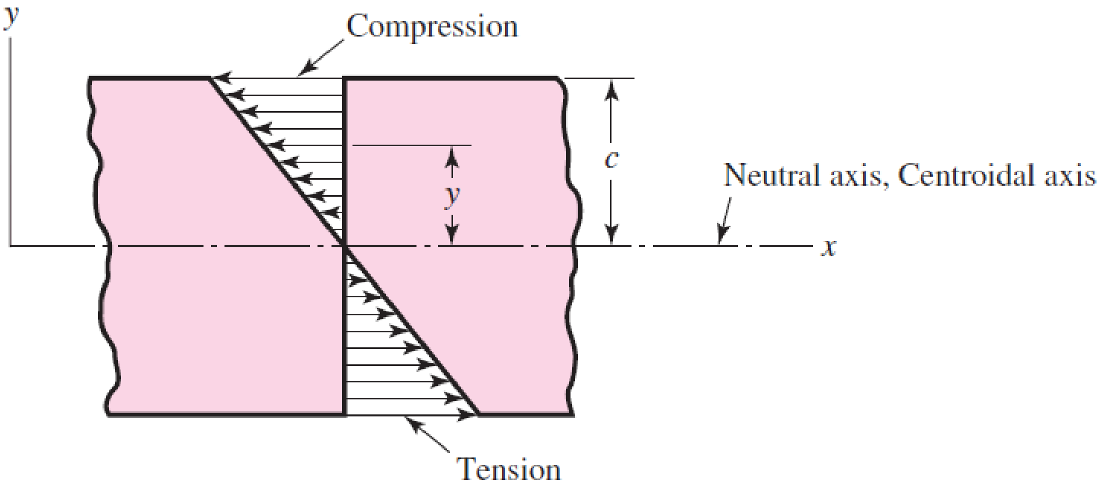

Figure 4 – Stress illustrated in a side view of a beam segment. Compressive forces are oriented into the face of the segment while tensile forces are oriented outwards from the face of the segment [1].

There are many important quantities embedded within the Euler-Bernoulli equation:

- w represents deflection
- $\frac{dw}{dx} = \phi$ is the slope of the beam
- $-EI\frac{d^2w}{dx^2} = M$ is the bending moment of the beam
- $-\frac{d}{dx}\left(EI\frac{d^2w}{dx^2}\right) = Q$ is the shear force in the beam

The deflection of the beam may be calculated using equation (3), derived from the Euler-Bernoulli equation, where the deflection (w) is desired. The equation requires the length of the beam (L), the Young's Modulus (E), the beam's loading force applied at the endpoint (P), and the moment of inertial cross-section (I). The moment of inertial cross-section, also known as the second moment of area, is a property dependent on the cross-sectional geometry, used to predict the resistance of a beam to bending and deflection about the axis that lies within the cross-sectional plane.

$$w = \frac{L^3}{3EI}P \tag{3}$$

The moment of inertial cross-section has units of (distance) ^{4} and varies based on the shape of the structure. The equation below, equation (4), shows the calculation for a beam of rectangular cross-section of width b, and thickness h.

$$I_\lambda = \int_A n^2\,dA = \int_{-\frac{h}{2}}^{\frac{h}{2}}\int_{-\frac{b}{2}}^{\frac{b}{2}} y^2\,dx\,dy = \frac{bh^3}{12} \tag{4}$$

Rewriting equation (3) for all known quantities, we see that only the deflection is unknown. This rewritten version is shown in equation (5). In a similar fashion, in an experimental setup, it is useful to determine the Young's modulus of an unknown material using this same equation. During an experiment, the deflection of the beam may be measured for a known load applied to a beam of known physical dimensions.

$$w = 4\frac{PL^3}{Ebh^3} \tag{5}$$

Assuming that all variables are known in equation (5), the strain at any point on the beam may be calculated. In order to calculate strain, more information about the beam must be calculated. The additional parameters which have useful information are the beam displacement at the point of interest, *w(x)*, and the bending moment of the beam at the point of interest, *M(x)*.

Firstly, the deflection of the beam along its length follows a quadratic function, expressed in equation (6). This simplifies to equation (3) at the loaded end of the beam where $x = L$. This expression is useful for determining how much flexure there will be at the point where the sensor is located, but is not necessary for calculation of strain.

$$\mathrm{w(x)} = \frac{\mathrm{Px^2(3L-x)}}{\mathrm{6EI}} \tag{6}$$

The bending moment of the beam is expressed in equation (7). This form of the equation is identical to that used to compute torque in the analysis of rigid bodies, where force is multiplied by the distance from which the force is acting. This parameter is directly used to compute the strain at a given point on the beam.

$$M(x) = P(L - x) \tag{7}$$

With the beam problem defined physically by the bending moment and geometrically by the moment of inertial cross-section, the stress at any point on the beam may now be computed. The expression for stress is described in equation (8), and it is obvious that it depends on both the position along the length of the beam as well as relative to the neutral plane of the beam. It can be seen readily that at the neutral plane, the expression for stress is described in equation (8a), and it is obvious that it depends on both the position along the length of the beam as well as relative to the neutral plane of the beam. It can be seen readily that at the neutral plane, *y=0*, and hence $\sigma_{mech} = 0$. The stress at any point along the beam also coincides with the location of the sensor at the farthest point from the neutral plane, c, as shown in equation (8b).

$$\sigma_{mech}(x, y) = -M(x)\frac{y}{I} \tag{8a}$$

$$\sigma_{mech,sensor}(x) = -M(x)\frac{c}{I} \tag{8b}$$

Finally, the stress is converted to strain using the relationship described earlier from Hooke's law. This procedure allows for the computation of mechanical strain on the cantilever beam when only the beam's physical dimensions and Young's modulus are known. The final expression for computing strain based on these parameters is given in equation (9).

$$\epsilon_{mech}(x) = -6\frac{P(L-x)}{Ebh^2} \tag{9}$$

1.2 Current Strain Sensor Implementations

Before discussing the possibilities for new designs, it is first necessary to explore the current state of the art for strain gauge technology. Currently, the most common type of strain sensor is the resistive strain gauge, fabricated on a flexible substrate using the deformation of a resistive wire trace to quantify strain. Other implementations include MEMS (*Microelectrical Mechanical Systems*), and microwave based designs. The previously mentioned design strategies will be discussed in this section in order to establish a baseline for the current state of the research area.

1.2.1 Resistive Strain Gauge

The strain sensor is a type of device with many commercial incarnations; however the most prevalent form of strain sensor implementation is the resistive foil strain gauge. As such, this thesis will use the resistive strain gauge as a benchmark for performance assessment. Resistive strain sensors are comprised of thin traces of a resistive metal atop a very thin flexible substrate. The metals used for this type of sensor are typically alloys which are corrosion resistant and are easily deformable. The most common examples of such alloys are Constantin and K-Alloy, which is aluminum based [2],[3].

The principle of operation for the resistive strain sensor is based in the fact that the resistance of a wire is proportional to length and inversely proportional to cross-sectional area, as shown in equation (10). As the length of the wire (l) is increased through tension, the cross section of the wire (A) is reduced, causing a net increase in resistance (R). Conversely, compressing the wire will cause the length to decrease and cross-section to increase, giving a net drop in resistance.

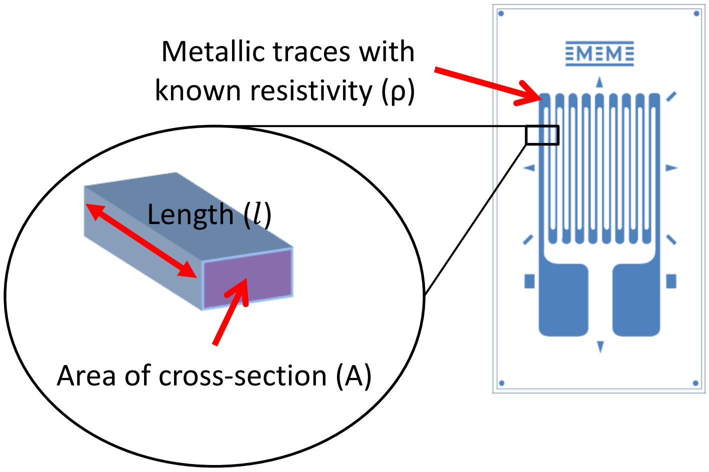

Figure 5 – Example of resistive stain sensor layout. The sensor is sensitive to strains along the long axis of the device. The resistance of the sensor varies linearly with the amount of deformation the sensor experiences.

$$R = \rho \frac{l}{A} \tag{10}$$

This change in resistance (ΔR) caused by deformation of the sensor is used as the quantifying measurement of strain for this type of sensor; however, the change in resistance must be converted to an actual strain for the sensor to be useful. As seen below in equation (11), the strain measured by the sensor (ε) is related to the resistive parameters, R and ΔR, of the sensor and scaled by a constant known as the Gauge Factor (*GF*). The Gauge Factor serves to scale the change in resistance, which varies linearly with applied strain, to a normalized strain.

$$\epsilon = \frac{\Delta R}{R \cdot GF} \tag{11}$$

To give an approximation for the magnitude of the change in resistance of the sensor, an inversion is performed, solving for ΔR using the above equation and manufacturer's data for a mid-range sensor. Assuming a maximum strain range of ±5%, a base resistance of 120 Ω, and a gauge factor of 2.125, the ΔR required is only 12.75 Ω. This value is quite small when compared to the nominal resistance of the sensor, leading to the necessity of a Wheatstone bridge to quantify the small change in output resistance.

This resistive type of sensor is capable of measuring strains of up to 10% assuming that the sensor is affixed using an appropriate adhesive. The nature of the physical layout of the sensor, with traces being very long along one axis, with very short transitions along the other, causes the sensor to be sensitive to strain primarily along only one dimension. This is a useful characteristic in that it allows the sensor to determine the direction of the applied strain. Several sensors can be arranged in a rosette pattern to offer an effectively directional strain sensor [4].

1.2.1.1 Resistive Strain Sensor Measurement

A Wheatstone bridge is used to measure minute changes in resistance, given its high sensitivity to extremely small changes in constituent component values. The Wheatstone bridge is essentially constructed as two parallel voltage dividers, arranged such that when the voltage at the output of each branch is equal, there is no voltage dropped across the bridge. In order to compensate for the variability of the individual component values, a potentiometer is used to ensure proper zeroing of the Wheatstone bridge. This allows for proper calibration and zeroing of the bridge output.

As any component value shifts away from the nominal point, the change in output voltage of one leg causes a voltage difference between the voltage dividers of the Wheatstone bridge. This is the voltage measured at the output of the bridge. The bridge voltage is related to the input voltage through the equation below, equation (12), in terms of the component resistance elements, shown in Figure 6. By adding a term for the change in the strain sensor resistance (ΔR), the equation can be rewritten and this term, the only unknown, may be solved for.

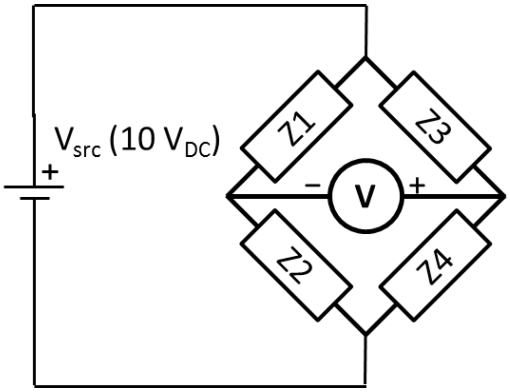

Figure 6 – Wheatstone bridge. The bridge is constructed of a pair of parallel voltage dividers. While the ratio of Z1/Z2 is identical to Z3/Z4, there will be no voltage across the voltmeter, V.

$$V = V_{in}\left(\frac{R_3+\Delta R}{R_4+R_3+\Delta R} - \frac{R_2}{R_1+R_2}\right) \tag{12}$$

$$\Delta R = \frac{V_{in}(R_2R_3 - R_1R_4) + V(R_1R_3 + R_2R_3 + R_1R_4 + R_2R_4)}{V_{in}R_1 - V(R_1+R_2)} \quad (\Omega) \tag{13}$$

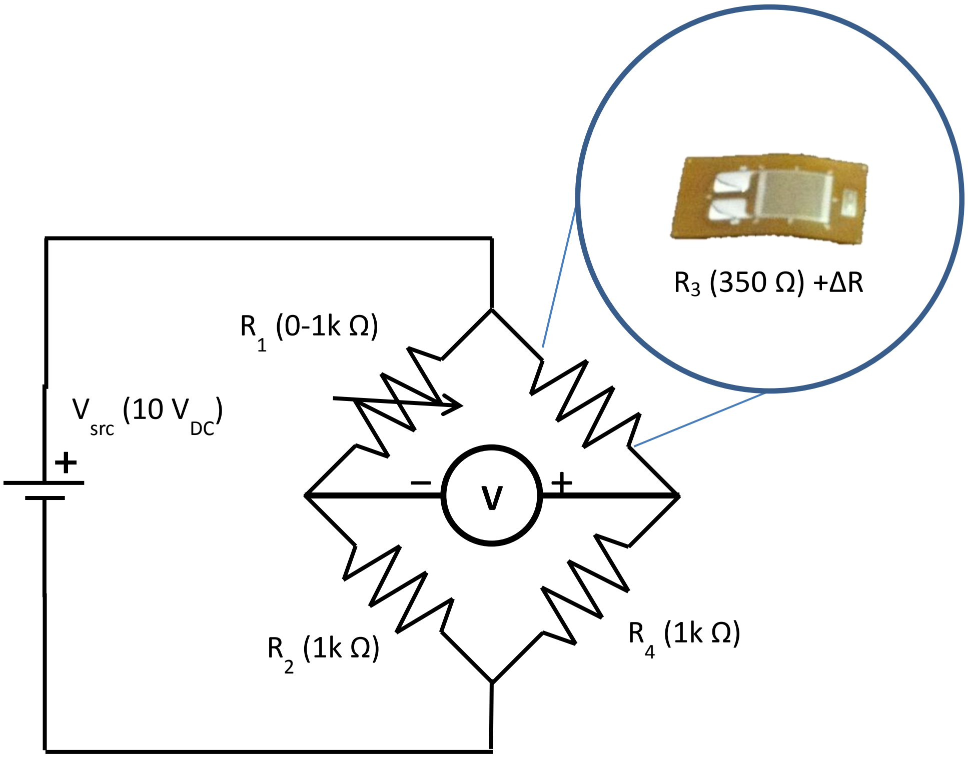

Figure 7 – Wheatstone bridge circuit with sensing element and potentiometer in place. The potentiometer is in place to allow for the tuning of the bridge for zeroing before measurements. The change in resistance based on strain is accounted for in the ΔR term.

A simple calculation of the expected bridge output voltage, *V*, will give insight into the sensitivity of the voltmeter required using the setup described above. The calculation is performed assuming a mid-range resistive strain gauge with a strain range of ±5% strain, and nominal resistance of 120 Ω, and a gauge factor of 2.125 [2]. From the explanation of the resistive strain sensor itself, 5% strain will correspond to a change in resistance of 12.75 Ω. It is then expected that the output of the Wheatstone bridge will be within the range of ±252.2 mV. This range is well within the measurement accuracy of the multimeter used for the experiment, which is capable of measuring accurately down to 0.01 mV.

Another figure of note is the current draw of the Wheatstone bridge. As the bridge voltage is dropped directly across the bridge, the resistance values that are chosen are important to ensure that too much power is not dissipated by the resistors, posing a risk for damaging or destroying components. All components in the circuit are rated for ¼ W power dissipation [2]. Assuming 10 VDC is dropped across a single branch of the bridge having resistance of 1200 Ω, the current expected in that branch is 8.4 mA. Using Ohm's law, this current corresponds to a maximum power dissipation of 0.069 W through a single resistive element, well below the ¼ W tolerance of the components used.

1.2.2 MEMS Based Strain Sensors

A definition of Microelectrical Mechanical Systems, *MEMS*, is "a device made from extremely small parts (i.e. microparts)" [5]. This regime of devices includes components such as inkjet printer nozzles, electronic gyroscopes, or compasses; structures and devices that are fabricated on a micrometer scale, with components ranging in size between 1 and 100 μm.

MEMS based strain sensors operate through one of two sensing mechanisms: detecting a change in resistance, or the change in capacitance, as shown below. The resistive version of the MEMS strain sensor has an identical method of operation as above with the sensor being a deformable resistive trace. The capacitive sensor, however functions based on the fact that as the carrying structure is strained, the sensor will be stretched or compressed, changing the inter-plate spacing and hence the sensor capacitance.

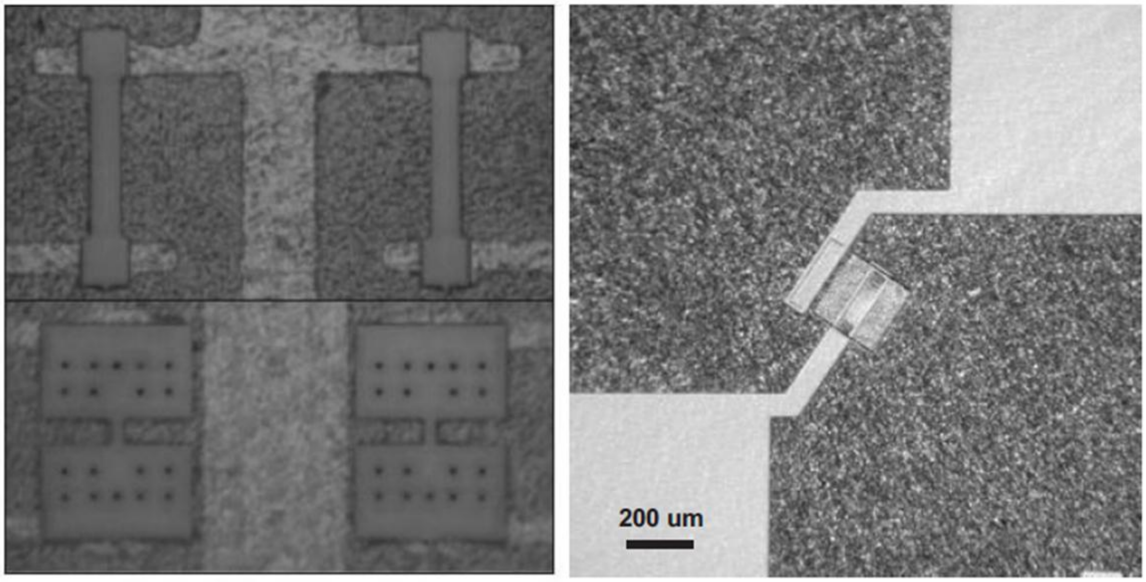

Figure 8 – Microscopic view of the MEMS based strain sensor. The sensor consists of a thin resistive film which deforms with applied strain [6].

The sensors developed using MEMS technologies have the advantage of being extremely small and fabricable directly on an integrated circuit or other silicon wafer. The inherent downside to such a layout is that the sensor is affixed to a very rigid structure. This means that the sensor will be excellent for applications such as strain measurement in small electronics devices, but will be capable of measuring only very small strains; an acceptable limitation when dealing with small scale electronics as they are usually very sensitive to the outside environment. Another benefit of the MEMS based sensor that is mentioned in the literature is that it may be implantable to monitor the strain, and effectively vibration, of bones or implants after surgery [6],[7].

1.2.3 Microwave Strain Sensors

There are also several types of strain sensors, which operate on the basis of electromagnetic phenomena, such as SAW (Surface Acoustic Wave) devices and a proposed use of metamaterials for sensing strain. These devices each have their own merit as strain sensing devices, which will be discussed in this section along with the inherent drawbacks to the implementation.

One major hurdle for microwave based sensors is that in order to extract the values of interest from the circuits constructed to measure strain, measurement equipment is necessary. The type of measurement equipment necessary for the device to relay the desired information to the user is quite important and must be considered in the determination of cost-effectiveness. In the case of the simple resistive strain sensor all that is required is a digital multimeter capable of better than millivolt accuracy. Any microwave device, however, will require a frequency source, a sweep generator, and a spectrum analyzer in order to measure the impedance or S-parameters of the device under test at a minimum. This up-front cost can be mitigated if the sensors themselves offer some advantage for the given application. In the case of microwave devices, the potential for performing measurements wirelessly may outweigh the cost of the test equipment required due to the freedom from wired connections, and the low cost of passive, printed circuit board implementation.

1.2.3.1 Wireless SAW Device

A SAW consists of an interdigital transducer (*IDT*) atop a piezoelectric wafer. These devices were originally intended for use as bandpass filters and delay lines as the speed of the wave propagation is much lower through the device than the speed of light and the spacing of the interdigital transducer’s fingers directly determines the frequencies allowed to pass through the device. By placing a reflector at the end of the SAW device, the surface wave generated in the SAW device is reflected back through the device and out through the inputs with a significant delay. The input/output of the device may be a antenna which passes the accepted energy through the SAW device and retransmits the return signal at the output [8]-[10].

Due to the frequency dependent nature of the IDT and the fact that substrate deformation will result in a change in the spacing of the fingers, the wireless SAW device performs well as a passive strain sensing device. Compared to this device, which has similar sensitivity to strain and an already wireless implementation, the SRR based strain sensor's main advantage is fabrication cost. While the SAW device must be fabricated on a piezoelectric crystal substrate, the SRR based strain sensor may be fabricated on a variety of substrates, using standard printed circuit board technology, offering a much cheaper solution for individual sensors.

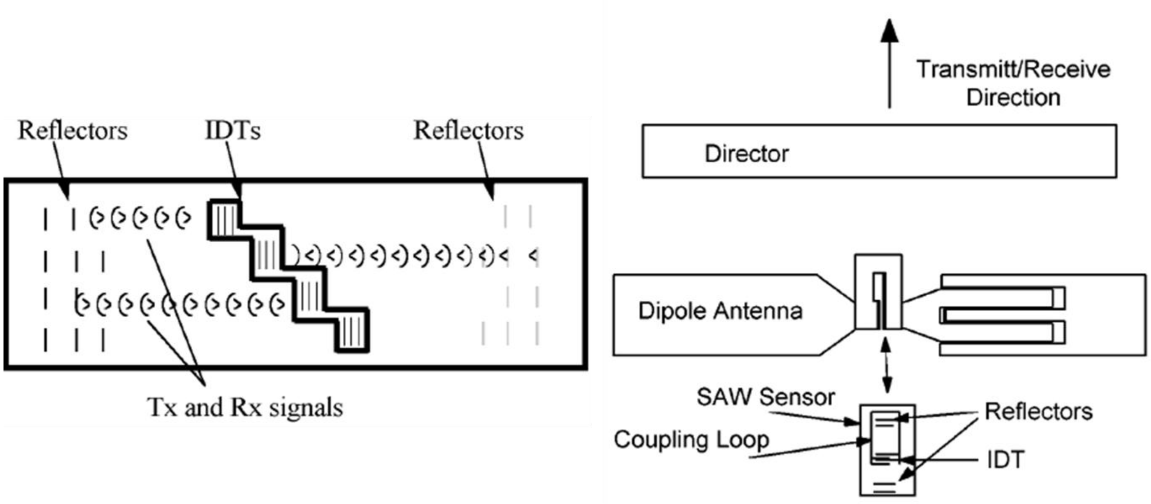

Figure 9 – Schematic overview of the SAW device based strain sensor. The device is both passive and wireless. The devices may be configured to have unique identifier codes [11].

1.2.3.2 Metamaterial Strain Sensor

The most promising current research in the area of metamaterial based strain sensing comes from a group at the University of Bilkent in Ankara, Turkey. These strain sensors are based more closely on the same principle of operation as the resistive strain sensor with stretching and compressing of the sensor causing the physical dimensions of the SRR to change [10], [12]-[15]. As will be shown later in the modeling section of this thesis, this mechanism is rather ineffective for sensing because while the SRR is very sensitive to changes in the substrate, the minute changes caused by stretching do not cause large changes in the resonance frequency, merely 5.148 KHz/microstrain for a sensor operating in X-band. This corresponds to a change of resonance frequency of a mere 4.3×10^{-4}%. While such small changes are detectable in ideal conditions with a very precise network analyzer, this is highly impractical for application as a sensor in real-world conditions.

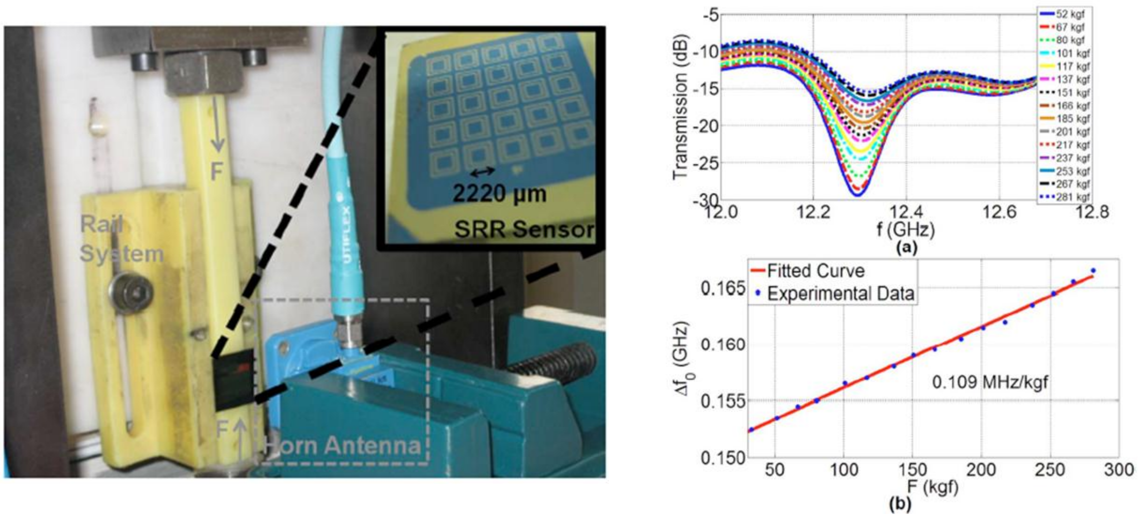

Figure 10 – Implemented SRR based strain sensor. The strain sensor described is capable of measuring small strains, however it has very limited sensitivity [15].

1.3 Metamaterials

Metamaterials are engineered materials which exhibit properties that are not normally occurring in nature. The word metamaterials comes from the Latin word "meta" meaning beyond used to modify "materials." They are engineered structures comprised of sub-wavelength inclusions used to alter the properties of another medium through their geometry rather than intrinsic material properties and are designed to generate specific effective material properties for various applications in acoustics, mechanics, and electromagnetics [16]-[22]. The interest in metamaterials for electromagnetics extends from optical devices such as cloaking of objects in the visible spectrum to super-lenses capable of sub-wavelength focal distances [20].

While there is great interest in optical metamaterials, the technology required to produce the devices themselves is just becoming available. This is due to the fact that by its very nature, the metamaterial is a sub-wavelength structure. Metamaterial structures are typically $\lambda/10$ in size, translating to approximately 50 nm for a structure designed to operate at 500 nm, or the frequency of blue-green light. The metamaterial itself is comprised of features much smaller than the structure as a whole. Assuming that the smallest feature dimension is 10% of the structure size, the final resolution required for fabricating a metamaterial device is now 5 nm, below the current fabrication limit for semiconductor devices. Because of this limitation, and the fact that microwave phenomena and optical phenomena are very similar, separated primarily by wavelength, microwave metamaterials have a much richer experimental base. The most interesting of these metamaterials operating in the microwave regime are based on variations of a simple structure, the split ring.

1.3.1 The Split Ring Resonator

The goal of this thesis is to address the feasibility of designing and fabricating a metamaterial based strain sensor. The basis of the design lies in the canonical example of the metamaterial, the split ring resonator (*SRR*) [20],[21],[23]-[29]. Comprised of concentric rings, each with a gap, the SRR behaves as an *LC* oscillator, with the ring itself acting as an inductance and the gap of the ring acting as a capacitance. There are studies in the literature explaining the physics of operation of the SRR and attempting to provide a mathematical model for its design [23], [24].

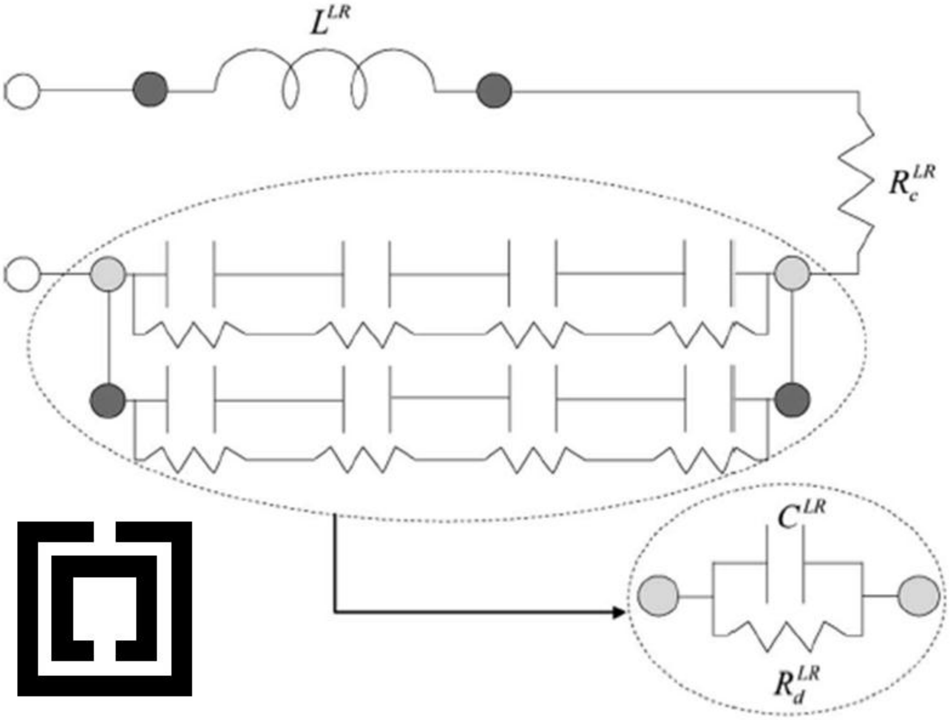

Figure 11 – Equivalent circuit of the split ring resonator. The resistive elements describe loss within the structure while the inductance and capacitance describe the structure's resonant behavior [23].

The modeling used in the design of the SRR for the implementation of a strain sensor or an antenna is based on defining an effective equivalent circuit for the device using the mutual impedance between rings as well as the impedance of the constituent rings [23]. From this mathematical modeling in conjunction with simulation, the approximate behavior of the SRR can be determined for use in implementing a viable design.

1.3.2 SRR Design Methodology

Bilotti, *e.t al* described the SRR, as well as several other metamaterial geometries using an equivalent circuit model which provides a fair approximation for the starting point in the design of an SRR structure. The "Bilotti model" takes into consideration the physical dimensions of the SRR: side length l, gap width g, line width w, inter-ring spacing s, and conductor thickness t, as well as the material properties of the metal and dielectric substrate on which the SRR is placed: substrate thickness h, relative substrate permittivity ε_r, conductor resistivity ρ_c, and substrate conductivity σ_c [23].

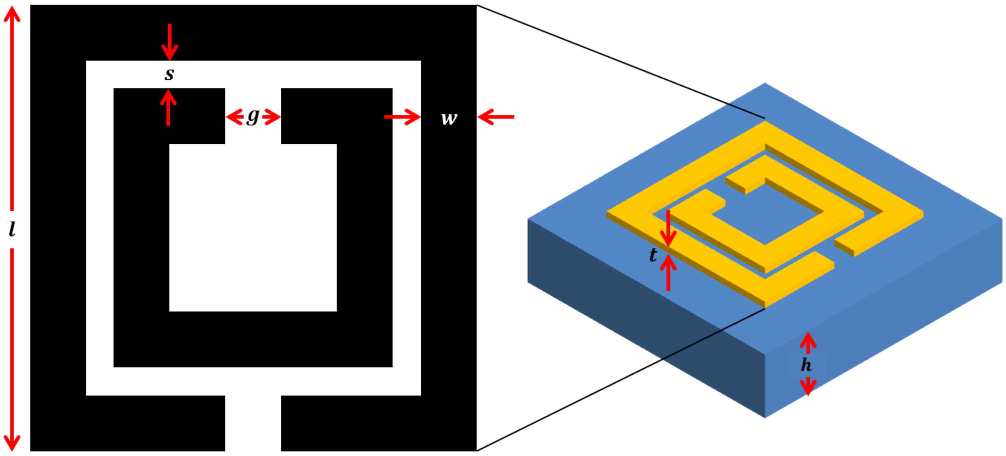

Figure 12 – Schematic view of the split ring resonator and all pertinent dimensions.

There are several disadvantages to using this model for the design of the SRR. This equivalent circuit, while good for approximate design, is less accurate at higher frequencies of operation. Another drawback from this model is that there are many inputs to realize a particular frequency of operation. This implies that for a given target frequency, there are many variations which could yield the same performance. Therefore, any given design may not be the absolute best design within the design space, but rather a local maximum relative to performance.

The Bilotti model is used as the basis for designing the SRR to operate at a target frequency of 10.8 GHz. The initial model results underestimate the resonance frequency, requiring some optimization of the resonance. From the initial design, finite element simulations of the final structure are performed to fine-tune the performance of the SRR to the desired operating parameters. This final sample has been previously fabricated and measured to verify its performance.

Table 1 – SRR design parameters and results from initial modeling using Bilotti model. The resonance is predicted to be close to 10.8 GHz

SRR Dimension		Material Properties		SRR Model Result	
$\boldsymbol{l}$	2.14 mm	ϵ_r	4.2	f_{SRR}	10.78 GHz
$\boldsymbol{g}$	0.25 mm	h	1 mm	L_{SRR}	8.046 nH
$\boldsymbol{s}$	0.30 mm	$\sigma_{substrate}$	$7.08 \times 10^{-3} S/m$	C_{SRR}	0.027 pF
$\boldsymbol{w}$	0.25 mm	t	0.03 mm	$R_{SRR,shunt}$	23.495 kΩ
$\boldsymbol{N}$	2 rings	$\rho_{conductor}$	0.017×10^{-6} Ωm	$R_{SRR,series}$	0.015 Ω

Table 2 – SRR design parameters and results from modifying initial Bilotti model in simulation. The SRR resonance frequency is underestimated. The actual resonance frequency of this SRR structure is closer to 10.8 GHz.

SRR Dimension		Material Properties		SRR Model Result	
$\boldsymbol{l}$	2.62 mm	ϵ_r	4.2	f_{SRR}	7.82 GHz
$\boldsymbol{g}$	0.46 mm	h	1 mm	L_{SRR}	11.203 nH
$\boldsymbol{s}$	0.30 mm	$\sigma_{substrate}$	$7.08 \times 10^{-3} S/m$	C_{SRR}	0.037 pF
$\boldsymbol{w}$	0.25 mm	t	0.03 mm	$R_{SRR,shunt}$	18.394 kΩ
$\boldsymbol{N}$	2 rings	$\rho_{conductor}$	0.017×10^{-6} Ωm	$R_{SRR,series}$	0.020 Ω

1.3.3 Scalability of the SRR

As with all microwave devices, the split ring resonator is capable of being scaled in order to operate at different target frequencies. Once an ideal design is obtained, it is simply a matter of scaling the device to resonate at the new desired frequency with a similar performance. For example, in order to shift the operating frequency of the SRR above, designed to resonate at 10.8 GHz, to resonate at 21.6 GHz, all dimensions would be scaled to 50% their original size. This is shown in the simulation below, where the result obtained above for the 10.8 GHz SRR are shown with the result for the 50% scaled SRR.

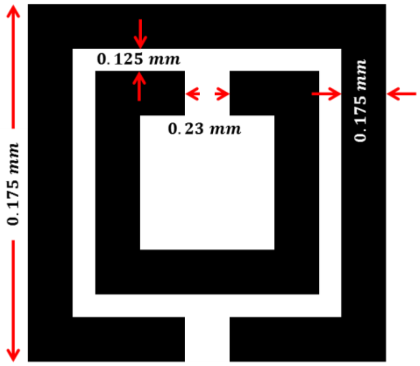

Figure 13 – SRR geometry when scaled to 50% of original size. The SRR is designed on an FR4 substrate, also scaled down in thickness by 50% to 0.4 mm. This SRR is expected to resonate at 21.6 GHz.

The resonance is not exactly double, as material properties do not remain constant across all frequencies. However, with minor rescaling, the new SRR can be made to resonate at exactly 21.6 GHz. The device resonates at 21.75 GHz, within 150 MHz or 0.7% of the desired frequency. This is especially useful when considering the possibility of miniaturizing of the SRR based strain sensor. From this simulation, it does indeed seem that by scaling the SRR based sensor from resonating at 1.7 GHz to 20 GHz is possible, and that the scaling factor would be approximately 1/11.8. This means that the scaled SRR sensor would be smaller than the resistive strain sensor it is being compared with. This possibility will be explored in greater depth in the future research chapter of this thesis.

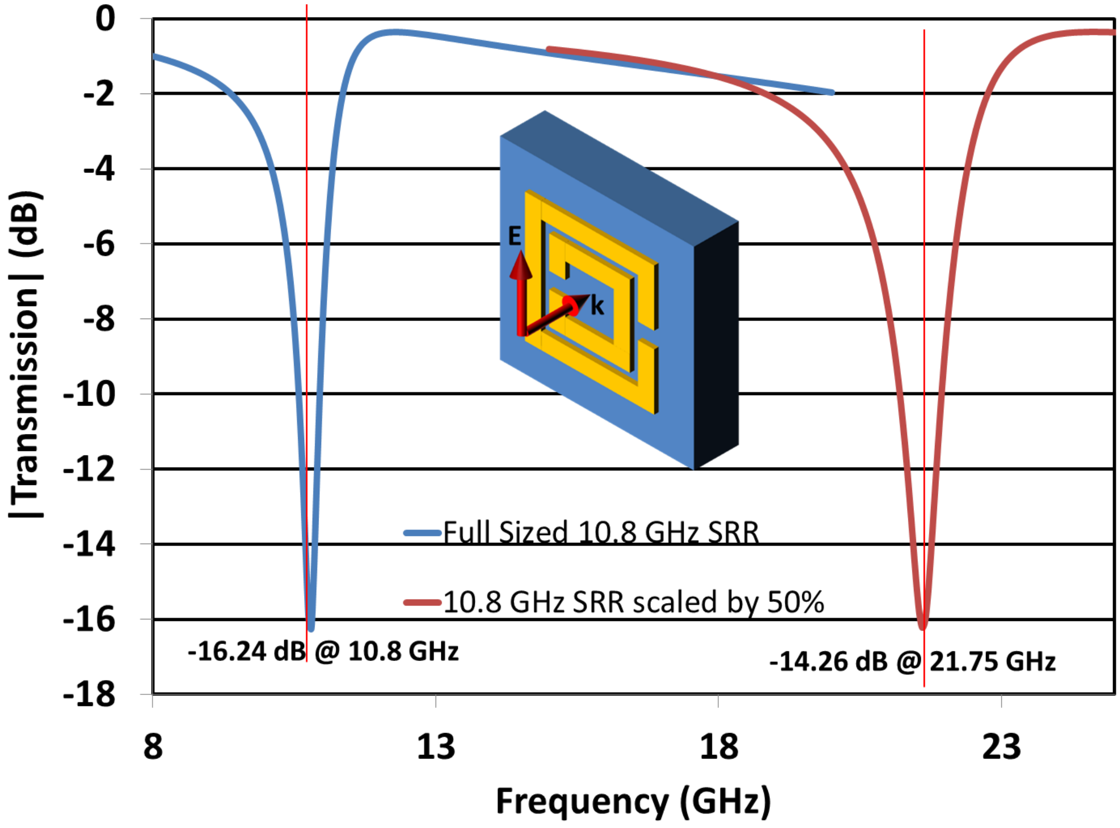

Figure 14 – SRR Resonance after scaling compared with original resonance frequency. The SRR now resonates at 21.75 GHz as opposed to 10.8 GHz. This is slightly higher than if the resonance frequency were simply doubled.

1.3.4 Effect of Substrate Dielectric Properties on Resonance of SRR

As mentioned previously, the resonance frequency of the SRR is very sensitive to its surroundings. The substrate on which the SRR is fabricated can shift the frequency of operation by extremely large amounts [25]-[29]. By loading the SRR with a substrate of higher dielectric constant, ε_r, and leaving all physical parameters constant, the resonance frequency will drop due to the structure becoming electrically larger. The converse is also true; if an SRR is moved from a high permittivity material to a lower permittivity material, the resonance frequency will increase.

In a previous study performed by Sheng et al., a sample comprised of split ring resonators was designed and studied, using measurement and numerical simulation techniques, to observe the effects of altering substrate permittivity and thickness. Their results, shown below in Figure 15, demonstrate that the resonance frequency may be altered in these ways, with the resonance frequency being shifted from 16 GHz to 6 GHz merely by altering the relative permittivity of the substrate material with no changes made to the actual SRR geometry, and shifts from 10.41 GHz to 10.24 GHz by making small changes in the substrate thickness [25].

Both of these effects are essentially the result of changing the effective material properties of the dielectric substrate, with the case of the thicker substrate effectively increasing the relative permittivity in the region behind the SRR. This dielectric loading will serve as the dominant effect used for the strain sensing application through the dielectric loading incurred by a changing air-gap in the substrate material.

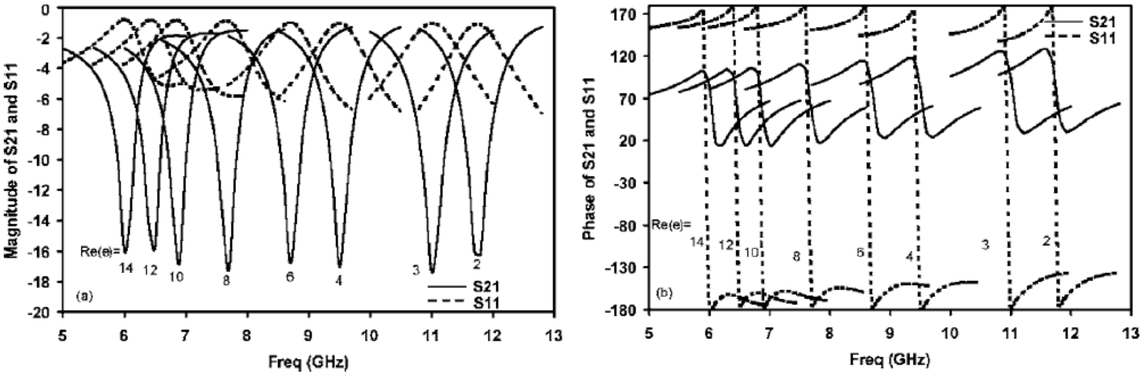

Figure 15 – Resonance frequency of the periodic SRR array as a function of dielectric permittivity. As the permittivity increases, the resonance frequency decreases. This effect is

useful in sensing applications as the dielectric loading presented by a variable air gap can change the permittivity of the sensor substrate [25].

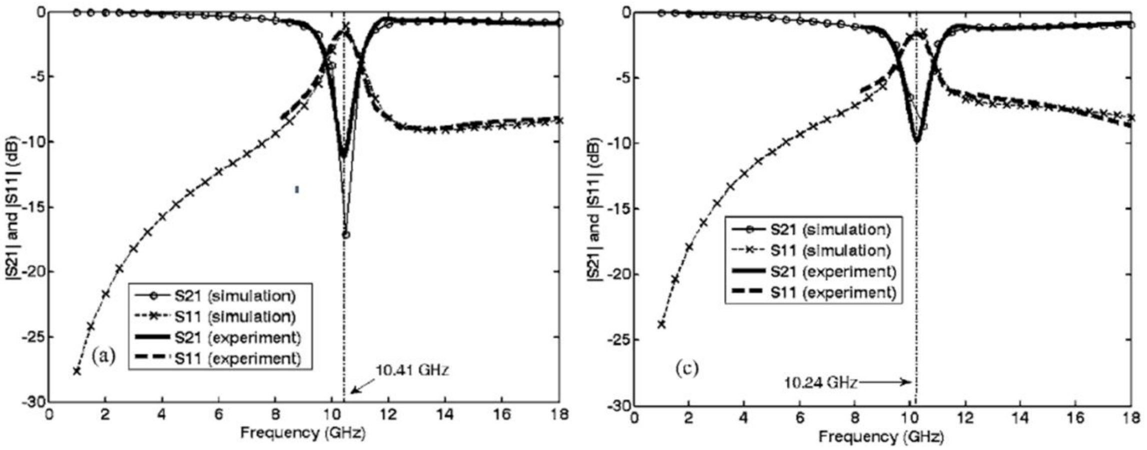

Figure 16 – Change in the resonance frequency of the SRR structure as substrate thickness changes. The resonance frequency shifts to the lower end of the spectrum as the substrate thickness increases. This is indicative of the dielectric loading effect [25].

1.4 Proposed Strain Sensor Implementations

The ultimate goal in proposing a metamaterial based strain sensor is the realization of a passive wireless sensor. By its very nature, the SRR is operating as a passive device, requiring no active elements for operation. As of this point, no successful design has been implemented yet. In this subsection, several attempts at implementing a version of the SRR based strain sensor will be discussed. Though some are unsuccessful at being implemented as sensors for various reasons, these devices demonstrate the same ability to alter resonance frequency of the SRR by manipulating dimensions of the device through stretching or the presence of air-gaps.

Another major consideration for the application to a real world sensing device is the overall cost of implementation. In order to perform measurements, there must be both a frequency source and a detector capable of operating in the frequency range of the sensor, while the resistive sensor requires much simpler, cheaper, DC voltage measurement equipment alone.

If the metamaterial based strain sensor were wireless, it would offer the benefit of being a completely passive device, essentially a sticker, which could be applied to the structure being measured, and a single detector could be used to measure many sensors. This type of implementation will allow for many cheap sensors to be installed with a single, more expensive, measurement device. The primary cost factor with any RF device operating at high frequencies is the cost of the frequency source. In this case, a 20 GHz Ku band source would be connected to an antenna and used to receive strain data from a wireless sensor. Ku band signal sources are prevalent in many police and military RADAR systems, especially for speed enforcement.

1.4.1 Dipole Coupled SRR Antenna as a Strain Sensor

After attempting to implement the aperture coupled SRR as a strain sensor, the next antenna to be tested was the dipole coupled SRR antenna. This antenna has extremely good performance as a nearly isotropic radiator and is highly sensitive to the gap between the SRR and feeding dipole [22]. This gap was exploited as the potential sensing mechanism for this implementation. Again, this antenna would be tested through a wired setup, however due to the device itself being an antenna, the interrogating antenna would simply scan for the frequency at which the sensor absorbed power.

The major drawback to this design is that in order for the antenna to be thin, there cannot be any form of a ground plane or metallic surface in the proximity of the device. This severely limits the potential applications for the device. Without the integration of a structure such as a high impedance surface, *HIS,* there is no means of overcoming this limitation. The HIS would mitigate the problem of proximity to a conductor by designing the sensor such that one is already present. The reasoning for requiring an HIS instead of a simple copper plate is that the reflected signal from an electrical conductor is 180° out of phase with the incident field, and unless the sensor is λ/4 thick, the reflection will all but eliminate the radiation from the device while a HIS has the benefit of 0° reflection, giving a required thickness of λ/8 [31].

The simulation results for the dipole coupled antenna implemented as a strain gauge are shown below. The results show that the antenna could potentially work as a sensor as there is some degree of resonance shift with increased displacement of the SRR. An unfortunate drawback to this design is that the resonance strength decreases as the displacement increases because the coupling mechanism which allows the antenna to operate also depends on the separation between the SRR and the dipole [22]. In this case, the SRR antenna could be designed to meet a compromise where the resonance is tailored such that reflection is minimal for the desired range of separations, but the feasibility is very low for this device as this hurdle as well as the guaranteed thickness both work against the use of this antenna as a sensor.

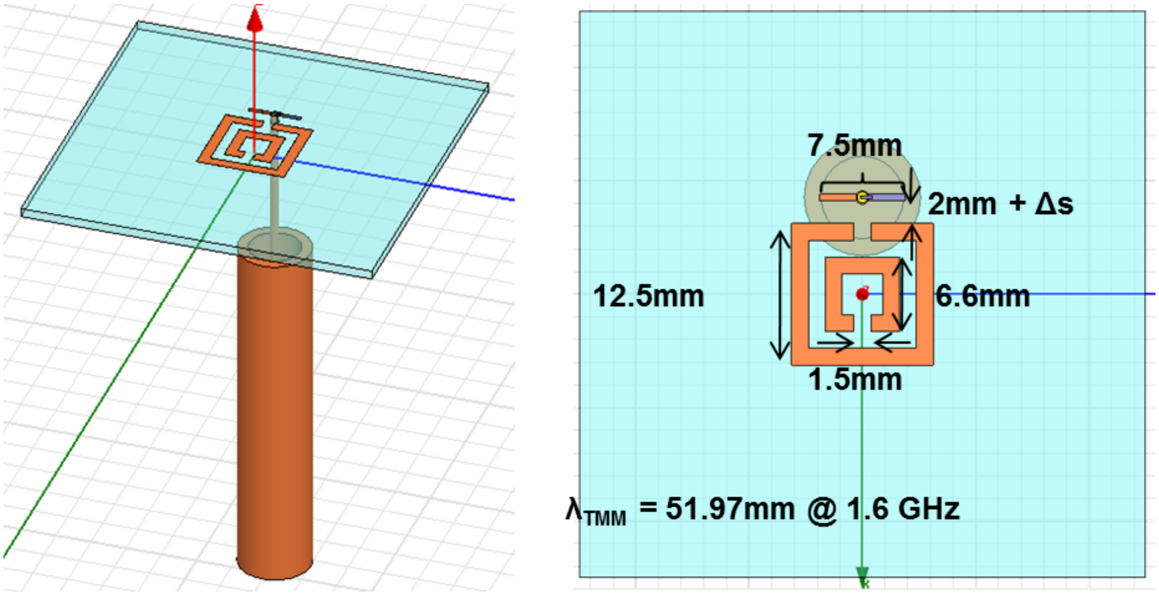

Figure 17 – The dipole coupled SRR antenna implemented as a strain sensor. For initial testing, only the gap between the dipole and the SRR is varied. In reality this would be the primary parameter to change as the substrate is much more flexible and elastic than the metal used for the antenna

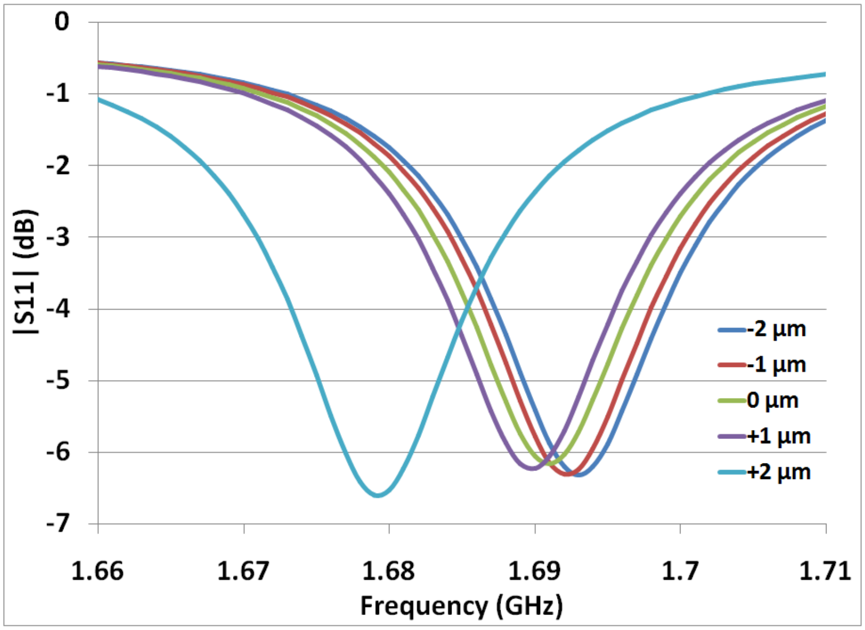

Figure 18 – Frequency response of the dipole coupled SRR when implemented as a strain sensor. The resonance frequency follows a general trend of reducing resonance frequency with respect to displacement of the SRR and dipole from their nominal position.

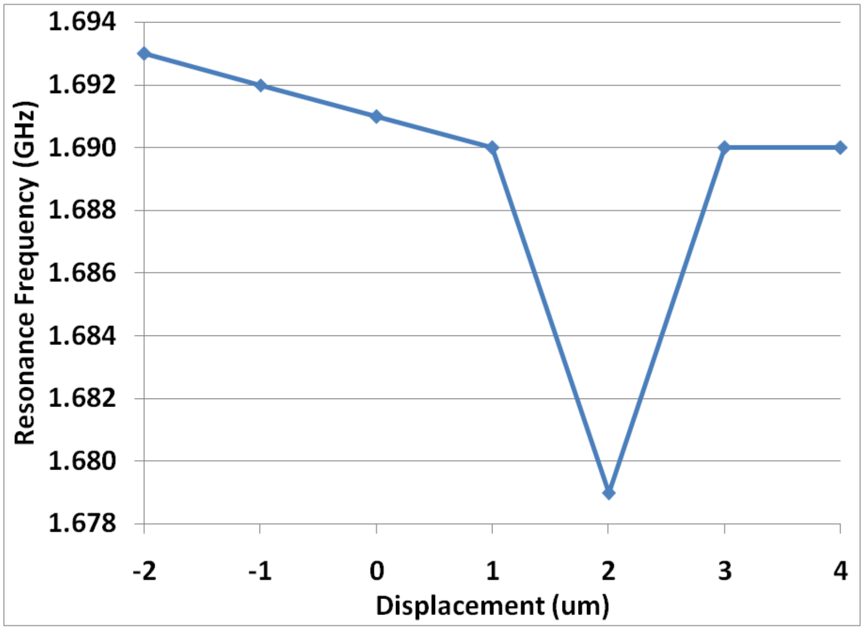

Figure 19 – Resonance frequency-displacement characteristic of the dipole coupled SRR antenna as a strain sensor. The sensor operates well as a sensor over a small range of displacements; however this implementation is impractical as it cannot be mounted on a metallic surface.

1.4.2 Passive Planar SRR Sensor

The implementation described by Melik, *et al.* in the introduction section of this thesis is has a layout which is quite favorable: a planar array of SRR arranged on a sheet which is used as a strain sensor. The primary problem with that implementation is that the sensing mechanism is not sensitive enough to be used in realistic conditions, with an expected resolution of 5.148 KHz/microstrain for an antenna operating in the GHz regime. An attempt to build off of this idea while still relying on a change in air-gap was simulated using HFSS. This structure, pictured in detail below is essentially a planar array of SRR on a Plexiglas substrate affixed in a similar manner as the aperture coupled SRR strain sensor, which had shown extremely favorable results, to an FR4 substrate with a copper backing. This sensor showed poor linearity for any practical range of air-gaps. Due to this, and the difficulty in implementing a sensor large enough to show a strong resonant response while still maintaining a somewhat uniform air-gap, the design is not viable as a strain sensor.

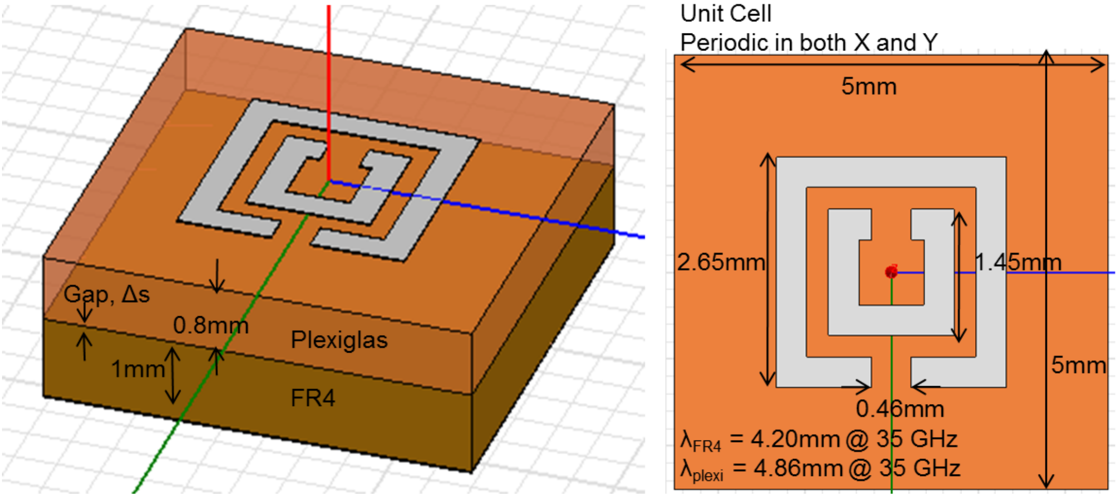

Figure 20 – SRR based strain sensor implemented as a hybrid between the design proposed by Melik, *et al*, consisting of a sheet of SRR, and the successful aperture coupled SRR design in hopes of realizing a passive, wirelessly readable SRR based strain sensor.

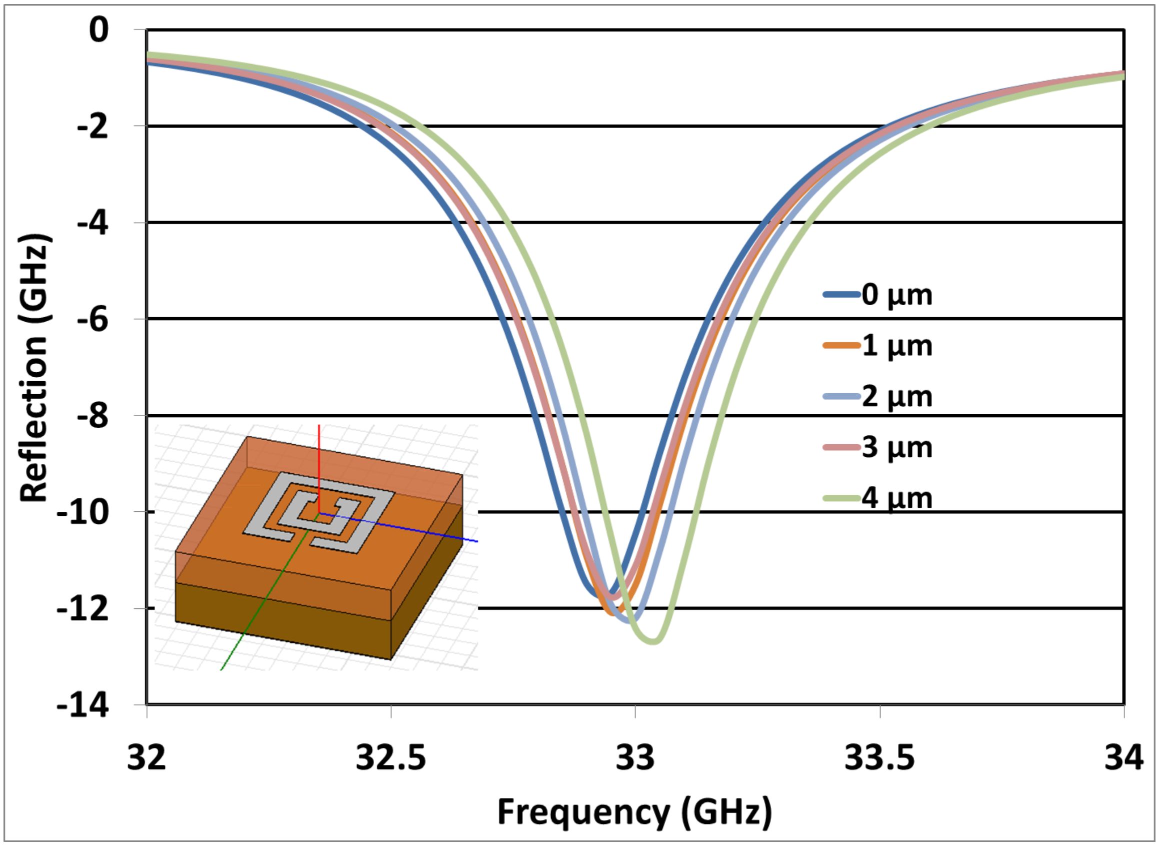

Figure 21 – Planar SRR based sensor sensitivity to air gap size. The air gap is between the two substrates, 0.8 mm beneath the SRR.

From the designs presented, the aperture coupled SRR antenna has the best functionality as a metamaterial based strain sensor. With future exploration into the effectiveness of the airgap as a form of dielectric loading and its effect on the resonance of the SRR, a passive wireless implementation may yet be possible to develop.

1.4.3 SRR Based Sensor Design

The metamaterial based sensor discussed in this thesis is comprised of a microstrip line coupled through an aperture in the ground plane to an SRR in order to provide a proof of concept for the mechanism of metamaterial based strain sensing applications based on a small air gap. This structure is based directly on the design of an aperture coupled SRR antenna with microstrip line feeding [31]. The sample is constructed of several layers, all of which are held in place through the use of nonmetallic bolts placed near the edges at the corners of the sample.

This type of bonding between layers will only ensure that the edges of the sample are in direct contact, leaving room for an air-gap near the center of the structure. This air gap is to be exploited as the sensing mechanism for the sensor application. As will be illustrated in this section, the SRR is extremely sensitive to its surroundings due to very high field localization [32]. This high localization is especially useful for sensing applications because it will allow for a relatively thin sensor due to dramatic changes in behavior being caused by changes in the structure near the SRR.

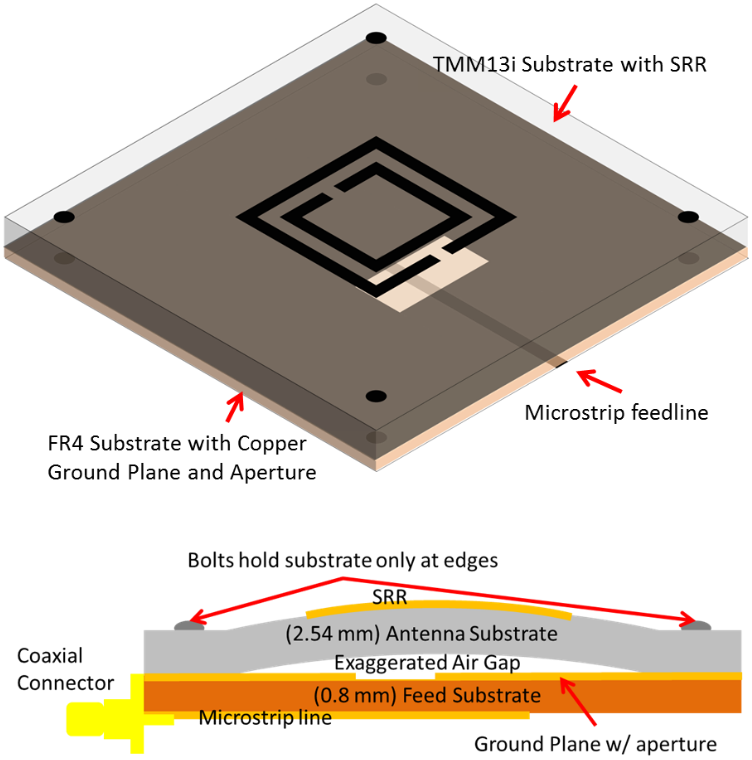

Figure 22 – Schematic view of the SRR based strain sensor. The upper layer of the sensor is affixed to the lower layer by four nylon bolts, one at each edge of the antenna. This allows for the creation of the air gap inside the antenna which is used as the sensing medium for the SRR based strain sensor. The dimensions of the SRR are as follows: outer edge length (*l*) = 19 mm, trace width (w) = 1.5 mm, ring gap (g) = 1.5 mm, ring spacing (s) = 1.5 mm, metallization thickness (t) = 17 μm for a target resonance at 1.575 GHz.

II. APERTURE COUPLED ANTENNA

The design which is implemented for the purpose of this thesis is based on an aperture coupled antenna with a metamaterial radiating element. In order to understand the fundamental principles of operation, some discussion on the aperture coupled antenna itself are presented. This subsection will discuss the design and simulation of the microwave structures and the aperture coupled antenna.

2.1 Modeling and simulation

As microwave structures become exceedingly complex, analytical solutions do not necessarily exist for the behavior of a given structure. In order to design complex systems such as antennas or metamaterials, numerical simulation becomes a necessity. The process by which microwave structures are modeled and simulated is discussed in this sub-section in order to explain the design steps and process flow of microwave simulation.

Ansys HFSS is a commercially available finite element simulation suite, which is invaluable for the design and simulation of complex structures which do not lend themselves to analytical solution. Ansys HFSS uses the Finite Element Method to discretize and solve Maxwell’s equations in their differential form. The solver breaks a structure into many tetrahedral mesh elements and explicitly solves the fields at the vertices of each tetrahedron in the form of a matrix. Interpolation is used to report the field result at any spot between mesh points. The accuracy of this method is determined by the size of the matrix and the precision to which results can be calculated. If these two constraints were able to be overcome for computation with a computer having infinite memory and precision, the accuracy of the finite element method could be infinite. A flow-diagram giving a high level description of how a user can design and simulate using HFSS is shown below [33].

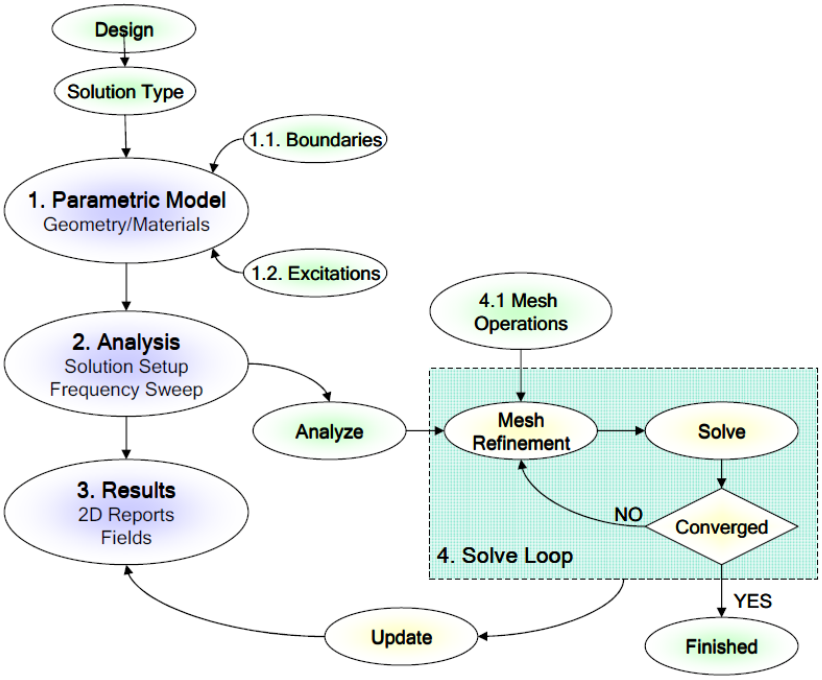

Figure 23 –flow diagram of the HFSS solution algorithm. Design is discretized and solved incrementally using the differential form of Maxwell's equations.

2.1.1 Boundary Conditions and Excitations

Any structure designed in a CAD suite, such as HFSS, is defined only over a very finite volume. HFSS compensates for this by applying a "background" boundary at the edge of the simulation region. By properly defining this boundary, the structure can be simulated as though it were radiating infinitely into free-space, inside of a perfect-electric-conductor, etc.

As mentioned earlier, HFSS uses the differential form of Maxwell's equations to solve the wave equations of the structure. For these expressions to be valid, it is assumed that the field vectors are single-valued, bounded, and have continuous distribution along with their derivatives [35]. Since a boundary represents a discontinuity, the derivatives of the fields are no longer continuous. By applying boundary conditions, the correct field behavior can be defined for a given interface.

In addition to boundary conditions, there must be some signal source in order to obtain any useful data. The excitations are placed at the points where the microwave signal, be it an incident plane wave, coaxial cable, or other type of feed, enters the system.

2.1.2 Microstrip Line Simulation Example

The microstrip line is the most prominent form of transmission line for RF and microwave devices due to its planar nature and simplicity of implementation on a single board. The microstrip line is also the simplest component involved in the design of the sensor, and as such, will be used as an illustration of the simulation process.

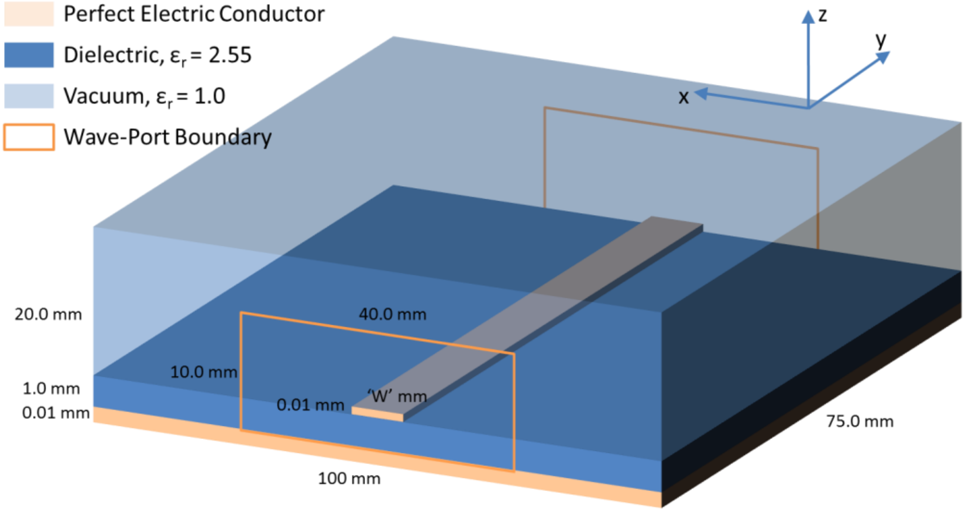

Microstrip Line Geometry with all dimensions. Radiation boundary conditions are applied along all edges of the dielectric substrate material and wave port boundary conditions are applied within the rectangle with an orange outline. By using a perfect-electric conductor for all metal surfaces, the metal-dielectric boundaries are defined.

2.1.2.1 Microstrip Line Theory

The substrate is assumed to be infinite in the direction perpendicular to signal propagation, and the line itself is defined by its width *W*, and the substrate thickness *B*. The characteristics of this transmission line are derived assuming a quasi-static approximation due to the fact that the line consists of a small trace above a dielectric, with fields present both in the air and within the dielectric rather than contained within the homogeneous dielectric alone as would be with a parallel plate waveguide. The design methodology presented here is based on numerical approximations and curve fitting to actual quasi-static solutions of the microstrip line problem.

Due to the air-dielectric interface and the fact that the fields of the microstrip line will be fringing through the air before entering the dielectric to reach the ground plane an effective dielectric constant is used to effectively replace the 2 media by a single homogenous medium. The effective dielectric constant is expressed by equation (19).

$$\epsilon_{eff} = \frac{\epsilon_r+1}{2} + \frac{\epsilon_r-1}{2}\frac{1}{\sqrt{1+12\,B/W}} \tag{19}$$

From this point, the microstrip line may be designed with either a fixed W/B ratio or a fixed line impedance.

$$Z_0 = \begin{cases} \dfrac{60}{\sqrt{\epsilon_{eff}}}\ln\left(\dfrac{8B}{W}+\dfrac{W}{4B}\right), & \dfrac{W}{B} \leq 1 \\ \dfrac{120\pi}{\sqrt{\epsilon_{eff}}\left[\frac{W}{B}+1.393+0.667\ln\left(\frac{W}{B}+1.444\right)\right]}, & \dfrac{W}{B} \geq 1 \end{cases} \tag{20}$$

$$\frac{W}{B} = \begin{cases} \dfrac{8e^{A}}{e^{2A}-2}, & \dfrac{W}{B} < 2 \\ \dfrac{2}{\pi}\left[C-1-\ln(2C-1)+\dfrac{\epsilon_r-1}{2}\left\{\ln(C-1)+0.39-\dfrac{0.61}{\epsilon_r}\right\}\right], & \dfrac{W}{B} > 2 \end{cases} \tag{21.a}$$

$$\begin{gathered} A = Z_0\sqrt{\frac{\epsilon_r+1}{2}} + \frac{\epsilon_r-1}{\epsilon_r+1}\left(0.23+\frac{0.11}{\epsilon_r}\right) \\ C = \frac{377\pi}{2Z_0\sqrt{\epsilon_r}} \end{gathered} \tag{21.b}$$

Using the previous equations, it can be determined that theoretically a transmission line having a W/B ratio of 1.0 would have a characteristic impedance of 94.4 Ω when designed for a substrate having relative permittivity of 2.25.

2.1.2.2 Assumed Properties

The line to be simulated is constructed using a substrate having a relative permittivity, ε_r, of 2.55. The relative permeability, μ_r, is assumed to be 1 as the substrate is nonmagnetic. The structure will be simulated with similar assumptions:

1. Thickness, *d*, of the substrate is 1 mm
2. Substrate width, *a*, of 100**b* is electrically large enough to be considered infinite
3. All metals (microstrip line, ground planes) are perfect electric conductors

Appropriate boundary conditions must be applied for the simulation to accurately represent the problem. The following types of boundaries/excitations were used:

Waveport Excitation

- The wave-port excitation was selected based on the fact that the input to this structure is placed at the edge of the simulation model, providing a matched input to the system. The waveport excitation is similar to the function of a port when performing network analysis. In the event of a microstrip line embedded within the model, a different type of port would be used that can describe how the field enters the model without being affected by other fields present within the model.
- There are general guidelines provided in the user's manual for the necessary dimensions of the waveport for the case of the microstrip line. A width of 10x the largest possible microstrip trace and a height 10x the thickness of the dielectric substrate were selected.

Radiation Boundary

- The radiation boundary is used in cases where waves have the ability to radiate infinitely into space. This is the case for any surface in the structure not making direct contact with a metal. It is crucial that the boundaries be defined as HFSS assumes by default that with no explicit boundary defined, the volume beyond the simulation domain is a perfect electric conductor.

- The radiation boundary should be placed roughly λ/4 away from the edges of any active elements. In this case, the ground plane and substrate are allowed to make direct contact with the radiation boundary, but it is assumed that the substrate is infinite, so no fields should be present at the simulation boundary far away from the microstrip line.

Air Box

- The air-box is not necessarily a boundary, but more a way of expanding the simulation volume to allow for the radiation boundary to be placed at the appropriate distance from the structure.
- The air box is assumed to be vacuum or air, with a relative permittivity of 1.0 and a relative permeability of 1.0.

2.1.2.3 Simulation Results for Microstrip Line Simulation

The simulation results shown below are for a parametric sweep of the microstrip line width. This is effectively a sweep of the W/B ratio as the substrate thickness is fixed at 1.0 mm. With the W/B ratio governing line impedance, each line configuration has a unique impedance. Due to the use of the wave-port excitation, the “input” to the microstrip does not have fixed impedance, but rather is matched to the line for minimal reflection. The plots below for S_{21} (Transmission Coefficient) and S_{11} (Reflection Coefficient) demonstrate that the microstrip line does indeed function as intended with extremely low reflection, near the noise level of the simulation, and very high transmission, near 100% or 0 dB. From the simulation, it is shown that the theoretical value of 94.4 Ω is quite close to the actual characteristic impedance obtained from full-wave simulation.

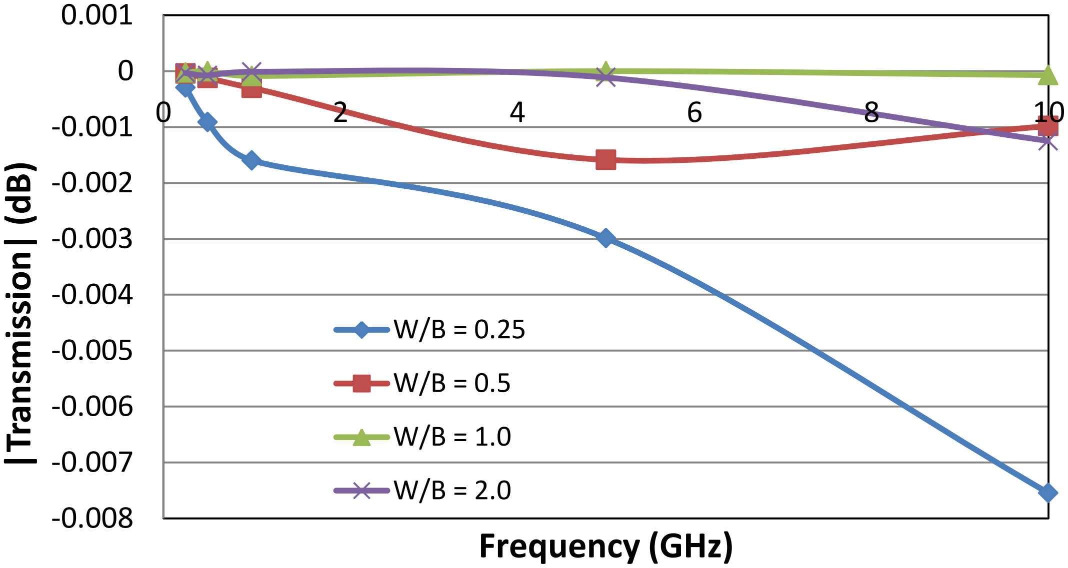

Figure 24 – Transmission coefficient amplitude for the microstrip line over several values of W/B. The performance of the microstrip line is extremely broadband, verifying the quasi-static approximation. Each W/B results in a unique line impedance.

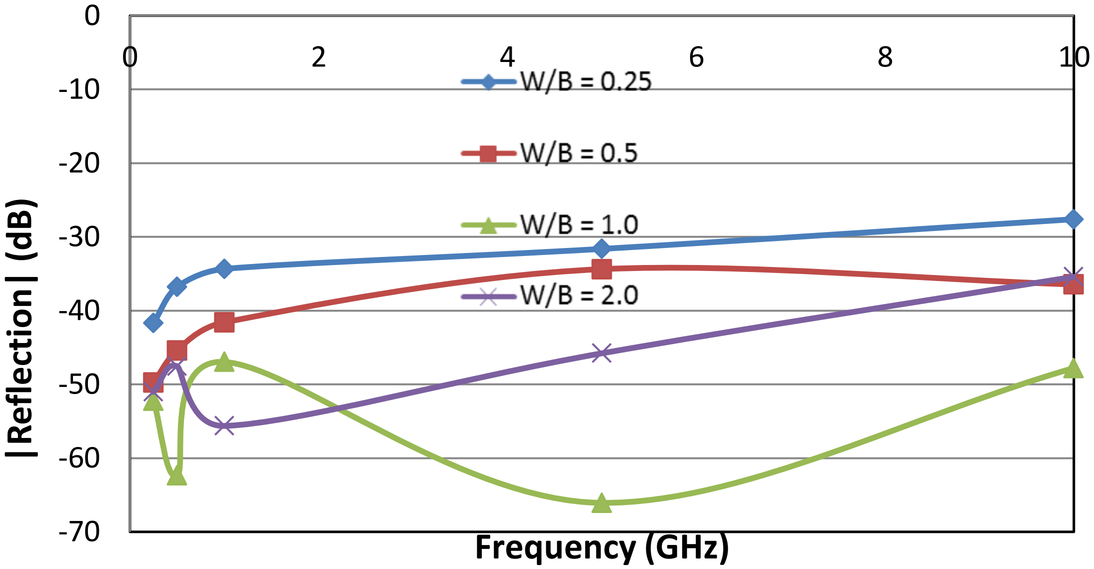

Figure 25 – Reflection coefficient amplitude for the microstrip line over several values of W/B. The performance of the microstrip line is extremely broadband, verifying the quasi-static approximation.

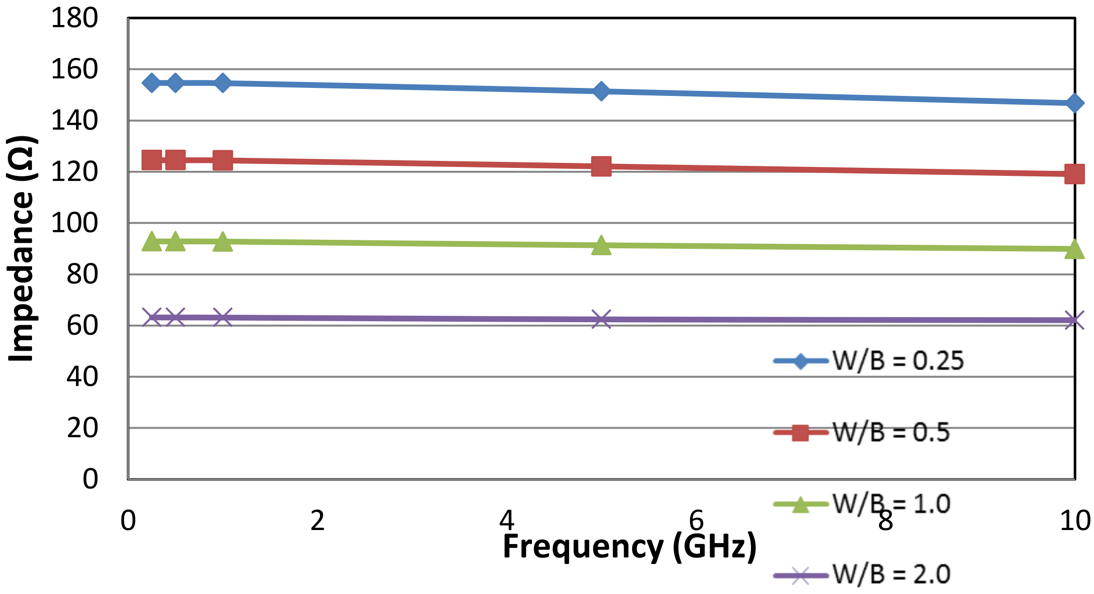

Figure 26 – Characteristic impedance of the microstrip line. Each W/B ratio corresponds to a unique impedance value.

2.2 Design and Simulation of Metamaterial Structures

The metamaterial based sensor in this thesis is originally the product of an attempt to create a metamaterial based antenna operating in the GPS frequency band [22], [31]. While experimenting with the antenna, it was noticed that pressure to the antenna caused a shift in the resonance frequency. Upon further investigation, it was determined that the shift was the effect of an air gap introduced due to multiple layers of material being used for a substrate material.

2.2.1 Simulated Structure Properties

The split ring resonator is assumed to be constructed of copper, with conductivity $\sigma = 5.8 \times 10^6$ S/m, corresponding to a resistivity $\rho = 1.73 \times 10^{-7}$ Ωm. Also, an FR4 substrate with relative permittivity of 4.2 is designed with a thickness of 1.0 mm. In order to evaluate the resonance characteristics of the SRR sample, the structure is assumed to be periodic in the plane of the SRR. This will have no effect other than allowing the simulation to assume an infinite plane wave being incident on the sample. The SRR is predicted to resonate at 7.82 GHz by the Bilotti model.

2.2.2 Simulation Results for Nominal SRR Sample

The simulated split ring resonator is actually resonant at 10.8 GHz, a frequency which is slightly different from the result predicted by the Bilotti model. This resonance behavior is also verified experimentally using freespace measurement techniques performed in X-band (8.2 – 12.4 GHz) [22]. This shows that using the Bilotti model, one will design for a frequency below the target resonance and then optimize the design after an initial simulation to achieve the final result.

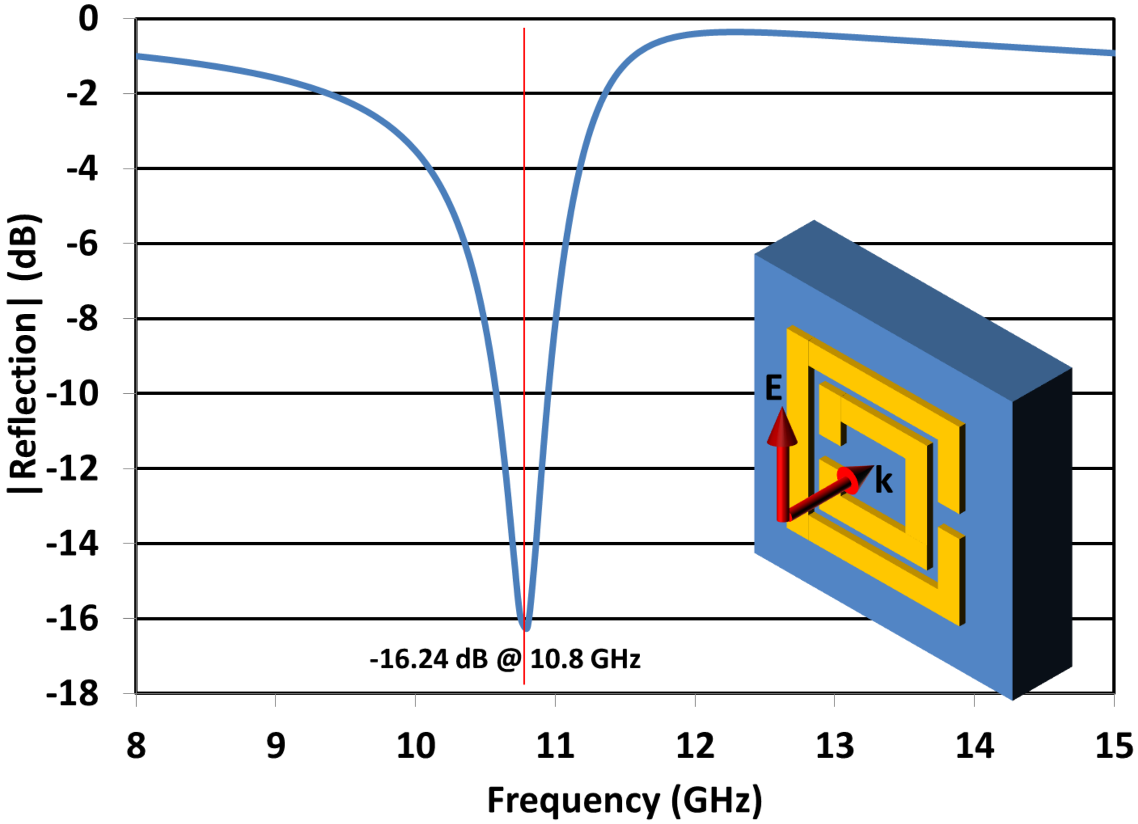

Figure 27 – Simulation result for the SRR structure. The E-field is parallel to the gap of the SRR, causing an electrical resonance within the structure.

2.2.3 Sensitivity of SRR to Fabrication Error

The split ring resonator is a device with a very high Q-factor; that is, the device has a very narrow, well defined, band of operation. As such, it is pertinent to examine how fabrication errors will affect the SRR's resonance frequency. The primary sources of error in fabrication come from the fabrication process itself. The SRR is fabricated using photolithography, a process in which a copper-clad substrate is selectively etched to leave behind the features of the SRR. The main advantage of this process is that it is very fast and low cost, while the drawback is somewhat low resolution and less than perfect edges on metal features. The image below, taken from a microscopic view at 10x magnification of a dipole coupled SRR antenna, shows how the fabricated structure does not have perfectly defined features as are assumed in simulation [22]. Subsequent remodeling of the SRR antenna taking into account these slight defects in the fabrication shows that somewhat minor defects in the fabrication of the SRR can cause resonance shifts of several MHz. The comparison below exemplifies this by comparing the frequency response of the pictured dipole coupled SRR antenna in simulation for the cases of an ideal design and with the fabrication errors observed through measurement under a microscope.

From the microscope view, it was measured that the traces are slightly narrower on the right side of the device by 141 μm. In addition to the gaps of the rings being shifted slightly, by 58 μm, the entire inner ring of the device is shifted by 33 μm to the right as well. These defects are quite small, but may have a large effect on the mutual impedance between the rings of the SRR. In addition to the slight shift, the SRR itself is not truly square, but rectangular, with an aspect ratio of 1:1.032. These errors cascaded together cause a shift in the resonance frequency of the simulated antenna by 25 MHz. From this shift, it becomes apparent that the fabrication of the SRR is sensitive to fabrication defects.

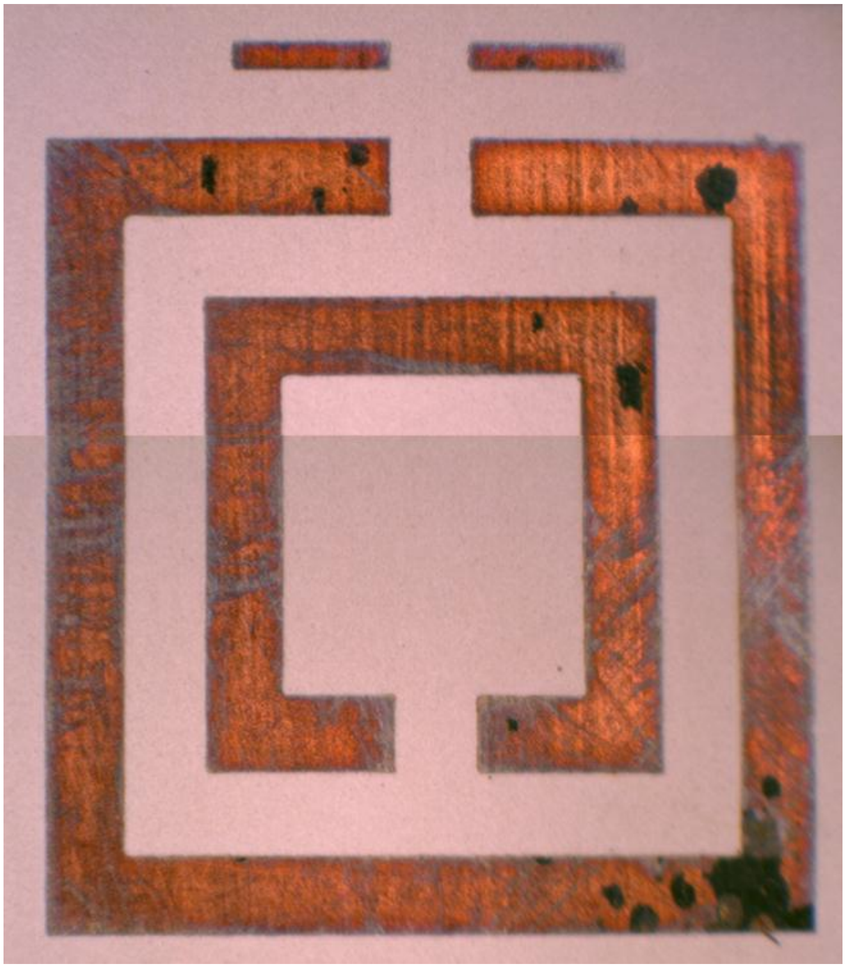

Figure 28 – Composite image generated from microscopic view of the dipole coupled SRR antenna before assembly. The antenna is slightly skewed and the gaps are slightly shifted to the right side of the image. This is likely due to the photo-mask not being perfectly flat during exposure.

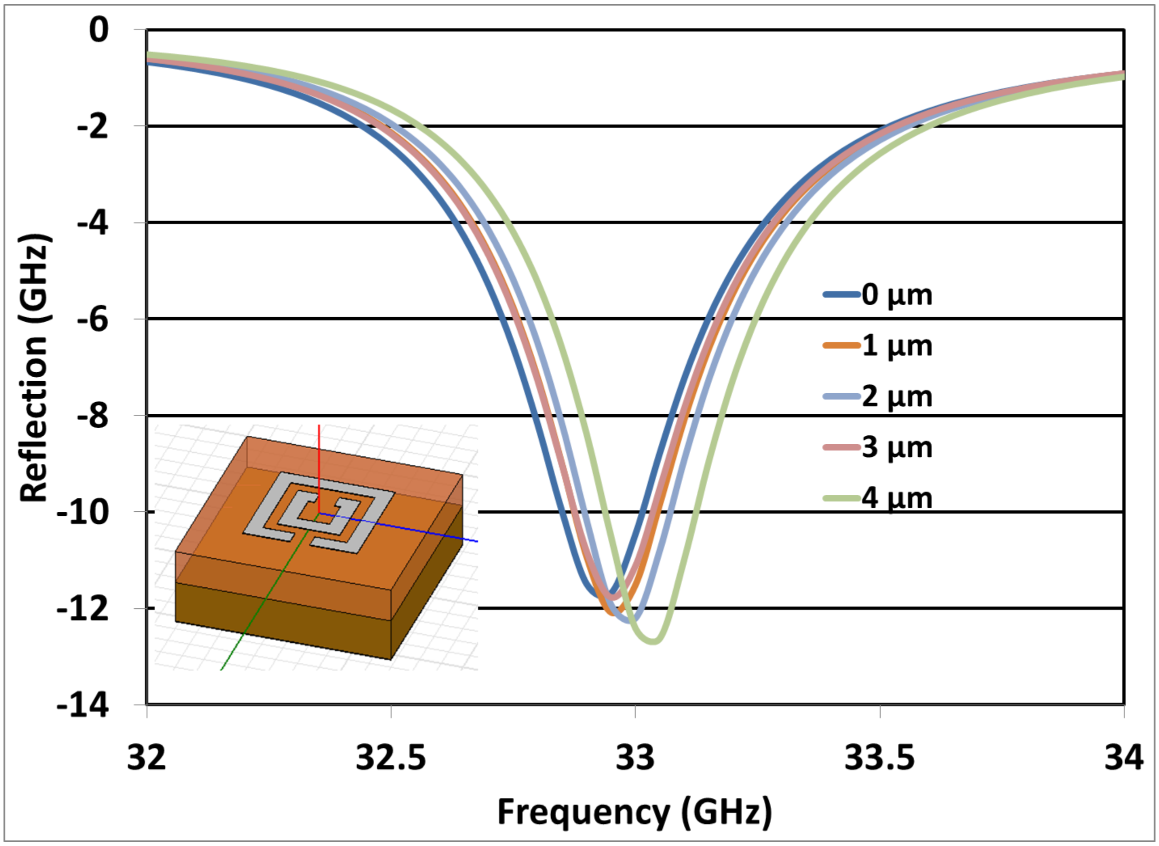

Figure 29 – Comparison between simulations for dipole coupled SRR antenna with ideal dimensions and dimensions measured after fabrication. The small defects in the fabrication cause a small shift in resonance frequency of the antenna.

2.3 Aperture Coupled SRR Antenna Design

The sensor discussed in this thesis is comprised of a microstrip line coupled through an aperture in the ground plane to an SRR in order to provide a proof of concept for the mechanism of metamaterial based strain sensing applications based on a small air gap. This structure is based directly on the design of an aperture coupled SRR antenna with microstrip line feeding [31]. The sample is constructed of several layers, all of which are held in place through the use of nonmetallic bolts placed near the edges at the corners of the sample.

The design and optimization of this antenna is quite complex. The design is carried out by optimizing an SRR to resonate at the desired frequency using the desired substrate, and separately designing a microstrip line feed to carry the signal to the antenna. From here, the designs must be merged and the aperture introduced. The individual elements served as a starting point from which the antenna design is generated [22], [31].

A benefit of this sensor being based on an antenna is that while the resonance frequency shift is being measured experimentally by the network analyzer through the reflection coefficient, S11, the same shift could also be detected by a remote antenna aimed at the sensor. The antenna has a radiation efficiency of 60.8%, as described in the antenna efficiency measurement section. This means that 60.8% of the accepted signal is radiated out into freespace for detection by another antenna. Even though the sensor would require an onboard signal generator, this implementation could be made wireless with no modifications to the sensor itself albeit requiring an onboard RF power source.

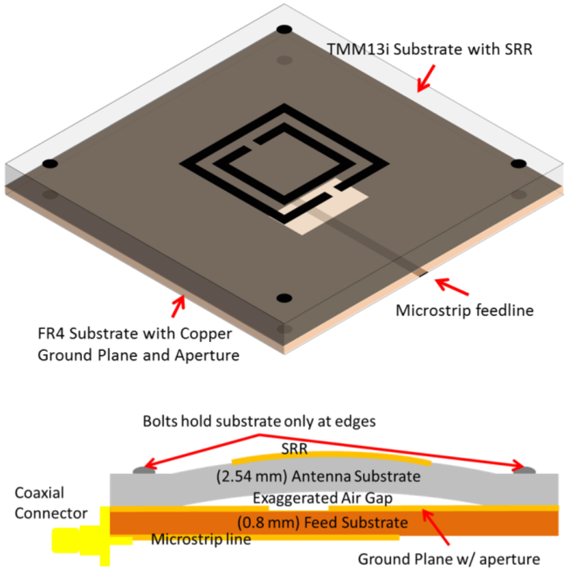

Figure 30 – Schematic view of the SRR based strain sensor. The upper layer of the sensor is affixed to the lower layer by four nylon bolts, one at each edge of the antenna. This allows for the creation of the air gap inside the antenna which is used as the sensing medium for the SRR

based strain sensor. The dimensions of the SRR are as follows: outer edge length (*l*) = 19 mm, trace width (w) = 1.5 mm, ring gap (g) = 1.5 mm, ring spacing (s) = 1.5 mm, metallization thickness (t) = 17 µm for a target resonance at 1.575 GHz.

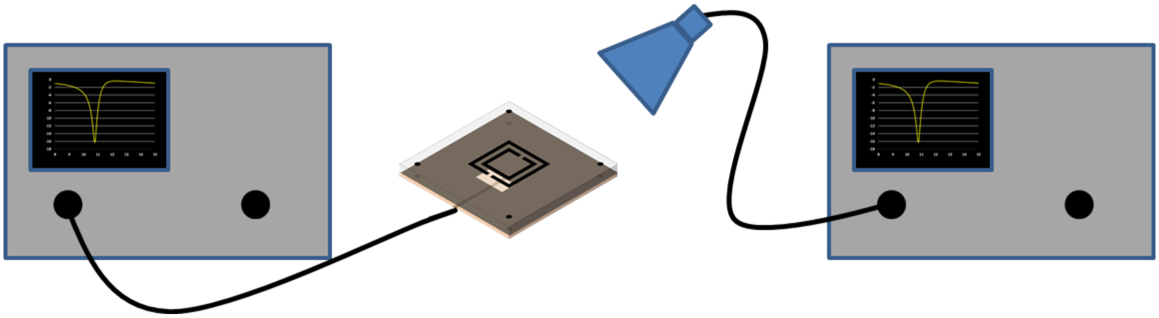

Figure 31 – Potential setup for reading strain remotely using the SRR based sensor as a powered sensor device. The device could be measured using a low-frequency horn antenna connected to a spectrum analyzer.

2.4 Microwave Measurements

The microwave devices used for experimentation for this thesis are measured using an Agilent E8363B *PNA* series network analyzer. The PNA is capable of full 2-port measurement of the S-parameters of the object under test. The S-parameters can be inverted to find the Impedance matrix of the device as well. In this case, the parameter of interest is the reflection coefficient, S11. The S11 parameter is used to determine the resonance frequency of the metamaterial based strain sensor.

At resonance, nearly all energy provided will be dissipated by the SRR through one of two mechanisms: radiation or loss. This sensor design is based primarily on an antenna, so a large amount of the input energy is radiated, as is explained in the sensor design section of this thesis. Loss is another large contributor to the energy dissipated by the SRR at resonance. This is due to the extremely high field localization very near the SRR, meaning that a material having dielectric loss tangent, *tan δ*, of 0.1% exposed to a field of 1000 V/m would see 10 V/m contributed solely to loss in the dielectric substrate [15]. While this measurement equipment is quite sophisticated and capable of performing very complex operations with the microwave signals that are transmitted/received, in a commercial type implementation, a simple sweep generator with a network analyzer would be capable of determining the operating characteristics of the SRR based strain sensor regardless of implementation: wired or wireless.

The PNA is calibrated using full 1-Port calibration, in which 3 calibration standards are used: short, open, and load. All microwave measurements are subject to errors introduced by the measurement device itself. The purpose of calibration is to remove as much of this machine introduced error as possible. The possible types of error encountered are directivity error, source match error, and reflection tracking error. These error source gains are solved for using the measurement results for each of the three standards.

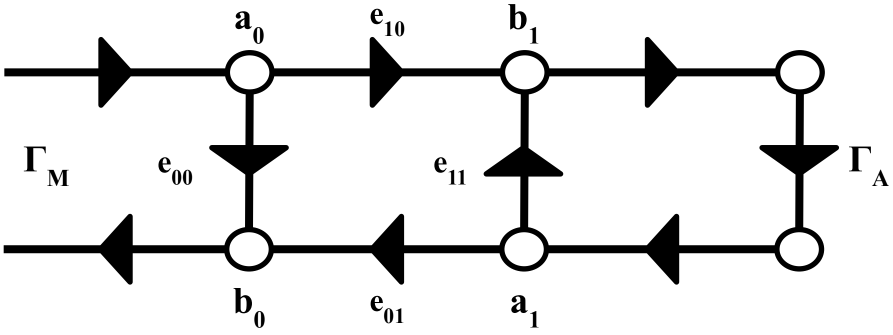

Figure 32 – Signal flow diagram for the 1 port calibration error model. The terms e_{10} represents the directivity error, e_{11} is the source match error, $e_{10}e_{01}$ is kept together as a single quantity representing the reflection tracking error. From this model, accurate measurements can be made using imprecise equipment given that the model parameters may be solved through calibration [34].

From the signal flow diagram above, the one port error model is described by equations (14)-(15). The solution of each case provides a linearly independent solution to the 3x3 matrix problem, resulting in the following linear system. Solving for each of the constants e_{00}, e_{11}, $e_{10}\cdot e_{01}$ and appropriately transforming the measured data, error can be removed.

$$\Gamma_M = e_{00} + \frac{e_{10}e_{01}\Gamma_A}{1-e_{11}\Gamma_A} \tag{14}$$

$$\begin{cases} a = e_{10}e_{01} - e_{00}e_{11} \\ b = e_{00} \\ c = -e_{11} \end{cases} \tag{15.a}$$

$$\begin{gathered} \Gamma_{A1}a + b - \Gamma_{A1}\Gamma_{M1}c = \Gamma_{M1} \\ \Gamma_{A2}a + b - \Gamma_{A2}\Gamma_{M2}c = \Gamma_{M2} \\ \Gamma_{A3}a + b - \Gamma_{A3}\Gamma_{M3}c = \Gamma_{M3} \end{gathered} \tag{15.b}$$

The problem with this method of calibration is that the standards used for the measurement are assumed to be perfect by the network analyzer, that is, they are truly an open, matched load, and short. In reality these standards cannot be perfect, and so some error still remains. Were the problem to involve 2 ports, TRL (*Thru, Reflect, Line*) calibration would be preferable as it does not depend on absolutely perfect standards, merely standards which are symmetric from both port 1 and port 2 of the network [34].

The particular sensor measured in this thesis' experimental section operates over a frequency range between 1.6 GHz and 2.0 GHz, centered just above the GPS Band (1.575 GHz); however a scaled down sensor implementation, described in the future works section, would require a source capable of operating over part of the Ku-band, from 18.0 GHz to 22.0 GHz. This source would be much more expensive than the low frequency source, however it is a necessity for a reasonably small SRR based sensor to operate.

2.5 Antenna Efficiency Measurements

The sensor implemented for this experiment is based on an electrically small antenna design. As such, the sensor, while technically wired, is still capable of transmitting the measurement result to a wireless receiver. The wireless receiver is beyond the scope of this thesis, as the primary focus is the proof of concept of the SRR based sensing mechanism; however, the ability to transmit measurements is of interest as it may provide insights into the implementation of a wireless sensor. The process of measuring the radiation efficiency of an antenna is described in this sub-section. The radiation efficiency will be useful in determining the required sensitivity of a receiver system, should one be implemented.

Radiation efficiency describes how well the antenna converts the power accepted into the structure into energy radiated into the far-field, defined as distances greater than $2D^2/\lambda$, where D is the largest dimension of the radiator and λ is the wavelength of the signal in freespace [35]. Harold Wheeler first proposed the method of using a perfectly conducting sphere to "short" the radiating fields in order to determine radiation efficiency in 1959 [36]-[39]. The Wheeler method, as it is known, consists of measuring the return loss of the antenna under test both inside and outside of a conductive walled cavity known as a Wheeler cap. The Wheeler cap has rough design criteria in that it must be of size $r \geq \lambda/2\pi$, but the cavity does not need to conform to any specific geometry [37], [38]. The simplest design, from a fabrication perspective would naturally be a cylinder, as copper pipe and end-caps are readily available in a variety of sizes. In the case of a cylindrical cap, this is essentially a section of circular waveguide which is shorted at both ends. It is important not to launch waveguide modes within the cavity, so the cavity must also be of small enough dimensions that all modes are evanescent. The lowest order circular waveguide mode, TE_{111}, shown below in equation (16), must be above the highest frequency to be tested within the Wheeler cap [34].

$$f_{cyl,TE_{111}} = \frac{c}{2\pi}\sqrt{\left(\frac{p'_{nm}}{a}\right)^2 + \left(\frac{l\pi}{d}\right)^2} \qquad (16.a)$$

$$f_{cyl,TE_{111}} = \frac{c}{2\pi}\sqrt{\left(\frac{1.841}{a}\right)^2 + \left(\frac{\pi}{d}\right)^2} \tag{16.b}$$

From the equation above, the resonance frequency of the lowest order mode that can be launched in the waveguide is 2777.4 MHz. This means that an antenna operating within or just above the GPS band will be acceptable for measurement using this Wheeler cap.

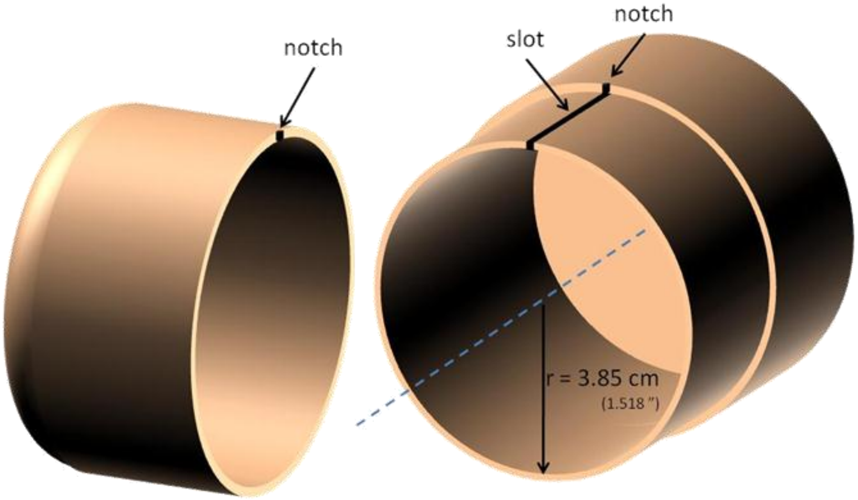

Figure 33 – Wheeler cap. The cap is slotted to allow the coaxial cable to be inserted into the cavity. After insertion, the upper portion of the cap is slid over the slotted section of the cap, leaving only a small hole for the coaxial cable to exit through.

The procedure for Wheeler cap measurements consists of making 2 antenna measurements: one with the antenna radiating into freespace, and the second with the antenna placed inside the Wheeler cap. These 2 measurements are used in conjunction with one another in a simple formula to invert the radiation efficiency of the antenna.

The Wheeler cap method assumes that the antenna has a single resonance and may be modeled using a simple RLC circuit, as shown below. This means that there are 2 possible configurations for the antenna, series and parallel.

In the case of a parallel resonance, all circuit elements are connected in shunt, and at resonance, the parallel impedance becomes maximum, essentially becoming an open circuit. Inside the cap, the radiation resistance is essentially removed, due to the antennas inability to radiate. This lack of radiation resistance is the only difference between the freespace and Wheeler cap measurements, and as the radiation resistance is removed, there is an inherent impedance mismatch for this measurement.

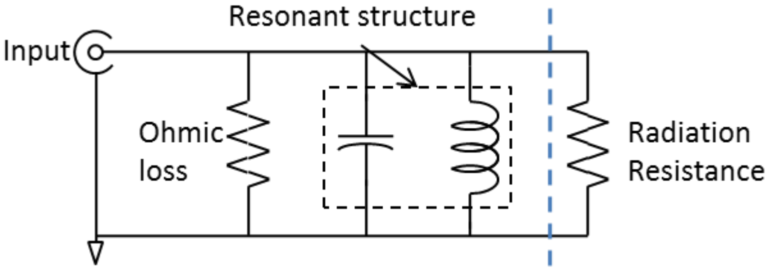

Figure 34 – Equivalent circuit for an antenna modeled using a parallel RLC circuit. The resonant block becomes an open circuit at resonance.

Going back to the antenna equivalent circuit, we see that without the reactive circuit elements in place, due to the resonance, the circuit is a classic example of a current divider. From this analogy, it is simple to see where the expression for the antenna efficiency comes. The efficiency comes from the amount of current which does not flow through the loss element in the circuit and is shown in equation (17.c).

$$e_{||} = \frac{R_{rad}}{R_{rad}||R_{loss}} = \frac{G_{rad}}{G_{rad}+G_{loss}} \tag{17.a}$$

$$e_{||} = \frac{G_{freespace}-G_{cap}}{G_{freespace}} \tag{17.b}$$

$$e_{||} = 1 - \frac{G_{cap}}{G_{freespace}} \tag{17.c}$$

For the case of the series resonant antenna, the model is the inverse. The series resonant structure becomes an effective short circuit, along with the radiation resistance when measured inside the cap. The derivation for radiation efficiency is now that of a voltage divider, with both resistances connected in series. The derivation is shown in expression (18.c).

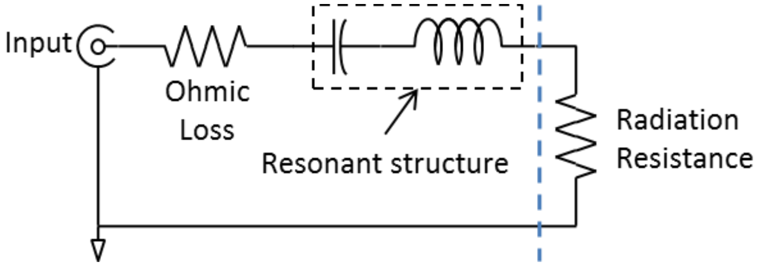

Figure 35 – Equivalent circuit model for antenna modeled best using a series resonant structure. At resonance, the resonant structure becomes a short and the radiation resistance is shorted inside the Wheeler cap.

$$e_{Series} = \frac{R_r}{R_r + R_{loss}} \tag{18.a}$$

$$e_{series} = \frac{R_{freespace} - R_{cap}}{R_{freespace}} \tag{18.b}$$

$$e_{series} = \left(1 - \frac{R_{cap}}{R_{freespace}}\right) \tag{18.c}$$

The measurement of most antennas requires special consideration to the fact that the feed may not be balanced. An example of an unbalanced antenna is a dipole, where there is a current flowing along the ground conductor back to the network analyzer. Ideally there would be no current flowing along the outer jacket of the network analyzer coaxial cable. This problem is mitigated in simulation through the assignment of the excitation. The ground conductor is forced to have zero potential, but in measurement practice this is not the case.

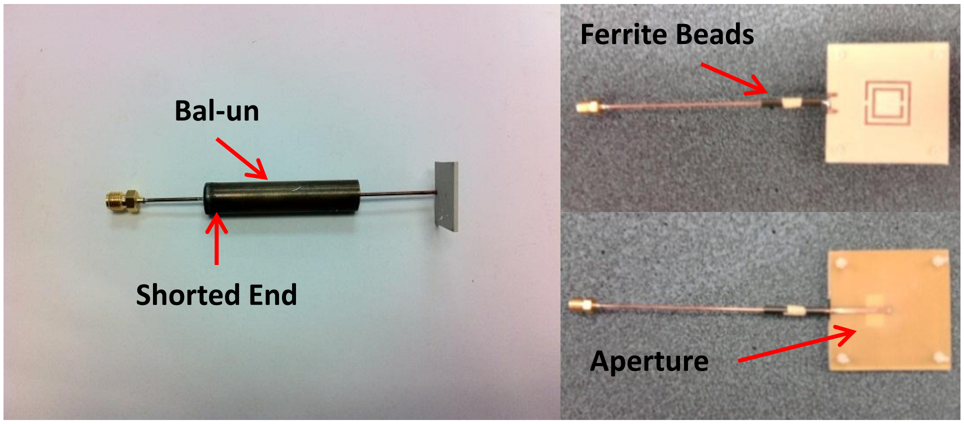

Figure 36 – Two means of preventing flow of current along return path of a coaxial cable. The bal-un is a λ/4 section of conductor shorted at the connector end of the cable which uses cancellation to eliminate back currents and the ferrite beads act as RF chokes, preventing the back-flow of current along the line.

The use of a bal-un ensures that there is no current along the outer jacket of the coaxial cable returning from the antenna to the network analyzer. The bal-un is constructed of a λ/4 section of brass pipe soldered to the outer jacket of the coaxial cable at the end farthest from the antenna radiator and bal-un operates based on the idea that any return current will travel down the jacket of the coaxial cable where it will encounter a reflector. After reflection, the return wave is 180° out of phase, causing cancellation of the current [40]. Approximately 1 cm of space is left between the back of the antenna and the bal-un to allow for placement inside the Wheeler cap for measurement.

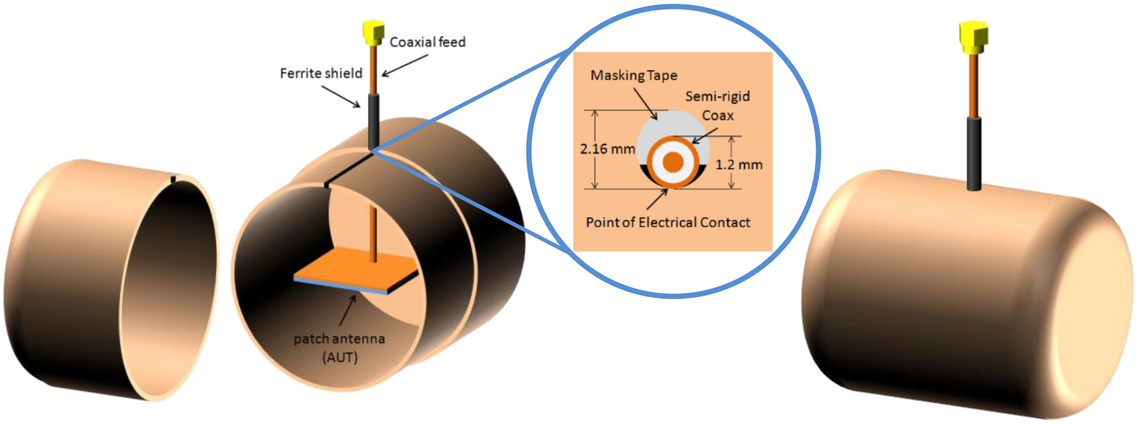

Figure 37 – Installation of antenna inside of Wheeler cap using ferrite absorber beads. The beads are left outside of the cap so as not to skew the measurement results.

As an alternative to implementing a bal-un, a ferrite absorber can be placed outside of the cap. This absorber works by blocking any return currents flowing along the outer jacket of the coaxial cable back to the network analyzer. It is not possible to perform Wheeler cap measurements with the absorber inside the cap as the absorber would skew the measurement results.

The freespace measurement is performed by connecting the antenna to the network analyzer and orienting the antenna such that it can radiate into freespace with minimal effects from nearby objects. Using the "port extension" feature of the network analyzer, a phase shift is artificially added to orient the root locus symmetrically about the real axis in the manner of an ideal RLC circuit as shown in Figure 39. From this, the input impedance of the antenna is recorded at the resonant frequency. This impedance should be purely real, or extremely close to being purely resistive. This value will serve as the freespace impedance and should be lower than the resistance of the cap measurement.

The antenna is installed in the cap in such a way that the bal-un is inside of the cap. This is because the Wheeler cap should be grounded, having zero potential. Before the bal-un, the antenna ground does not necessarily correspond to the same ground reference used for the network analyzer. The same procedure as for the freespace measurement is performed with the port extension being added to shift the root locus to the ideal RLC. The impedance at resonance is also recorded for this case and will serve as the “inside cap” measurement.

From here, the SRR antenna radiation efficiency is computed using the parallel circuit model. This model was selected by noticing that the freespace input impedance was lower than the impedance measured with antenna in cap.

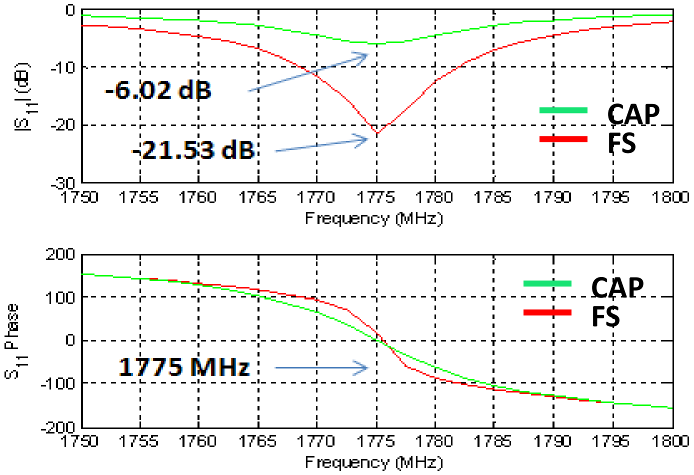

Figure 38 – Return loss plot for the aperture coupled SRR antenna. The phase delay added from the port extension causes a zero-phase crossing at resonance.

Table 3 – Experimentally obtained values from Wheeler cap measurement. The measured efficiency is slightly lower than the simulated efficiency due to inevitable fabrication defects opposed to an ideal model

Antenna Parameter	**Value**
Resonant Frequency	1775 MHz
|Return Loss|	21.53 dB
$Z_{freespace}$	58.71 + j2.71 Ω
$Z_{wheelercap}$	149.94 + j3.54 Ω
Radiation Efficiency	**60.84%**
Simulated Efficiency	**74%**

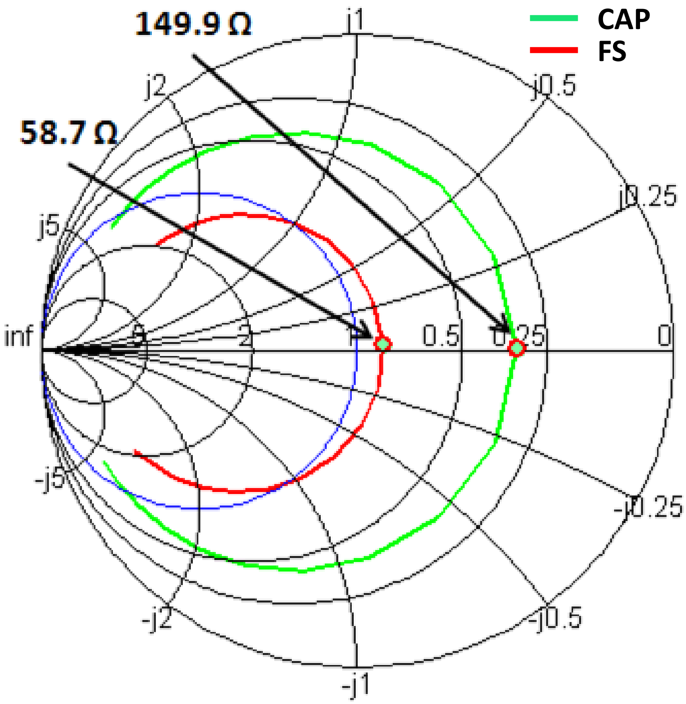

Figure 39 – Smith chart plot of the antenna input impedance for both cases of with cap and without cap of the aperture coupled SRR antenna. The resonance loops are symmetric about the real axis with the actual resonance frequency for each case marked. The freespace impedance is much lower than the cap impedance, indicating that the antenna has a parallel equivalent circuit.

Of course, the artificial phase shift is introduced arbitrarily by the experimenter, and as such, could be added or modified after the measurement using data processing techniques to ensure that the resonant loops remain symmetric. This approach is actually more reliable than relying solely on the experimenter's judgement of what is symmetric. In order to implement such a routine, a MATLAB script was written which selected several pairs of frequency points on opposite sides of the resonance frequency to compare. In an ideal RLC circuit, these impedances would be complex conjugates; that is an impedance of 50 + j6 Ω at 5 MHz above the resonance should correspond to an impedance of 50 – j6 Ω at 5 MHz below the resonance.

Several points are needed because with a real system, a single pair is not enough to judge symmetry as slight variations may arise at the point selected.

III. SRR BASED STRAIN SENSOR

A major consideration for the application to a real world sensing device is the overall cost of implementation. In order to perform measurements, there must be both a frequency source and a detector capable of operating in the frequency range of the sensor, while the resistive sensor requires much simpler, cheaper, DC voltage measurement equipment alone. If the metamaterial based strain sensor were wireless, it would offer the benefit of being a completely passive device, essentially a sticker, which could be applied to the structure being measured, and a single detector could be used to measure many sensors. This type of implementation will allow for many cheap sensors to be installed with a single, more expensive, measurement device. The primary cost factor with any RF device operating at high frequencies is the cost of the frequency source. In this case, a 20 GHz Ku band source would be connected to an antenna and used to receive strain data from a wireless sensor. Ku band signal sources are prevalent in many police and military RADAR systems, especially for speed enforcement.

3.1 Aperture Coupled SRR Strain Sensor: Sensitivity to Varying Air Gap

The relationship between frequency shift and measured strain is critical to the determination of the performance of the SRR based strain sensor. In this subsection simulation is carried out to determine the effect of inducing small air-gaps between the substrate carrying the SRR and the ground plane of the device.

The resonance is expected to shift as the air gap changes based simply on the knowledge that the SRR is extremely sensitive to substrate properties. Assuming a homogeneous substrate composed of the air-dielectric mixture, it is clear that as more air is present, the effective dielectric constant will lower due to a decrease in the high permittivity substrate per unit volume.

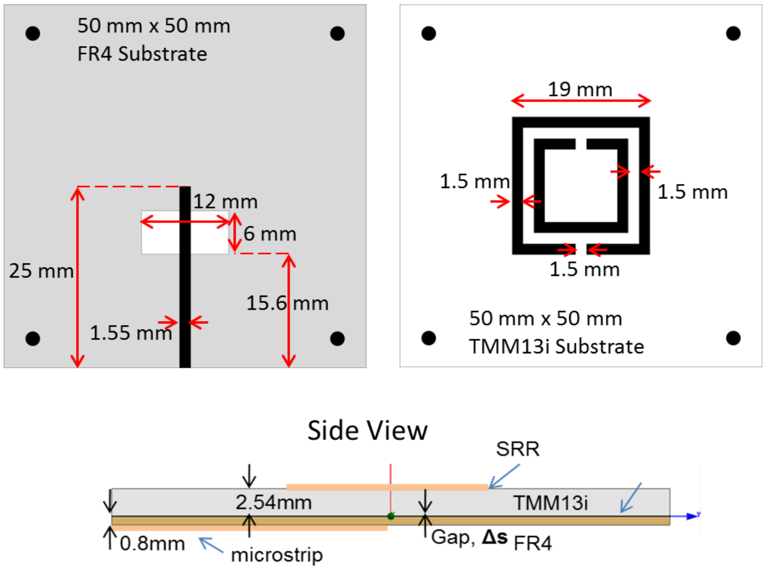

Figure 40 – Schematic view of the SRR based strain sensor as simulated in HFSS. The air gap is directly between the ground plane of the microstrip line and the TMM13i SRR substrate.

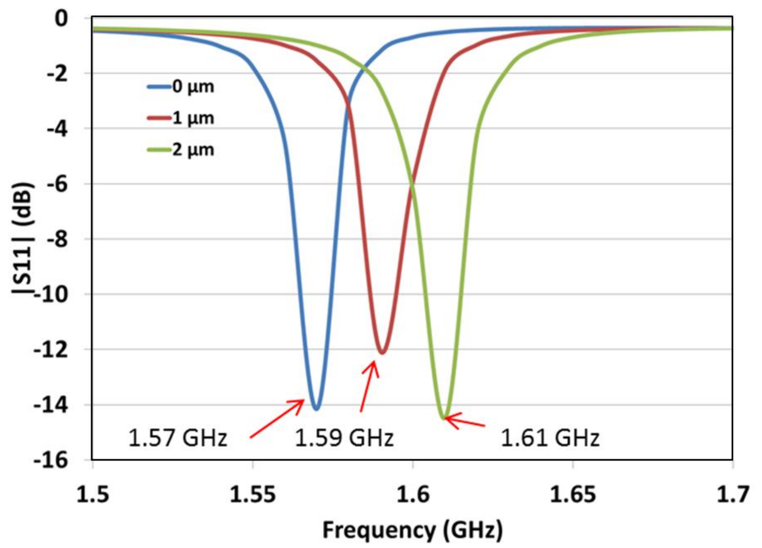

Figure 41 – The frequency response for several air gap sizes between the SRR substrate and the ground plane. While the frequency of operation changes, the resonance strength remains somewhat constant.

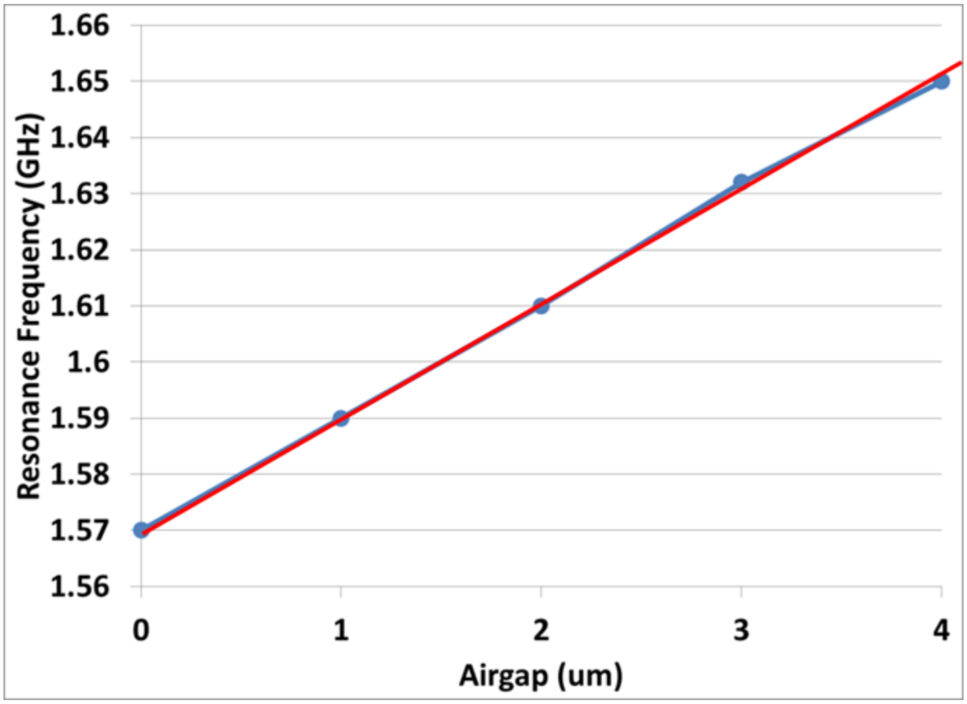

Figure 42 – Resonance frequency of the SRR with respect the size of the airgap between the SRR substrate and the ground plane of the microstrip. The relationship is extremely linear, indicating that the sensor will track well over a reasonable range of airgaps.

From the simulation results shown above, the SRR resonance frequency has extremely good tracking with respect to the size of the air gap and is promising for the application to using this change as a sensing mechanism. As the air gap becomes smaller, the resonance frequency should increase. This means that when the sensor is under tensile strain, the upper substrate will be stretched, and hence, reduce the air gap, causing a decrease in resonance frequency. The inverse can be inferred for the case of compressive strain, where the upper SRR substrate will be compressed and forced outward, increasing the air gap and raising the resonance frequency.

3.2 Miniaturization

The sensor which was experimentally implemented in this thesis is, at is heart, an antenna designed to operate in the GPS frequency band. As such, the sensor used for testing is physically quite large, while electrically, the sensor is reasonable small small, 0.26λ x 0.26λ. This means that due to the scalability of microwave devices, given the same material properties, the design should scale down linearly with operating frequency. By increasing the operating frequency from 1.575 GHz to 20 GHz, the device should ideally scale from 50 mm x 50 mm x 3.34 mm to 3.975 mm x 3.975 mm x 0.236 mm. This is actually 21.75% smaller than the resistive strain sensor used in this experiment.

Simulation, shown below, for the sensor after scaling show that the resonance frequency does not scale exactly, material properties are not necessarily constant with frequency, however, as the study of air gap size indicates, the sensor will still perform adequately, with the resonance frequency shifting linearly as a function of air gap size over a relatively large span, from no gap present to a gap thickness of 2% the total substrate thickness, or 4 μm. After the 4 μm mark, however, the resonance begins to shift back to lower frequencies.

Regardless of the nonlinearity, it would still be possible to use the device as a sensor with displacements ranging from 0 μm to 7 μm as the frequency response is varying monotonically. A polynomial fit would allow for the approximation of the resonance frequency for any given gap within the range. This could then be inverted back to a quantifiable strain, though the inversion would no longer be a simple linear relation.

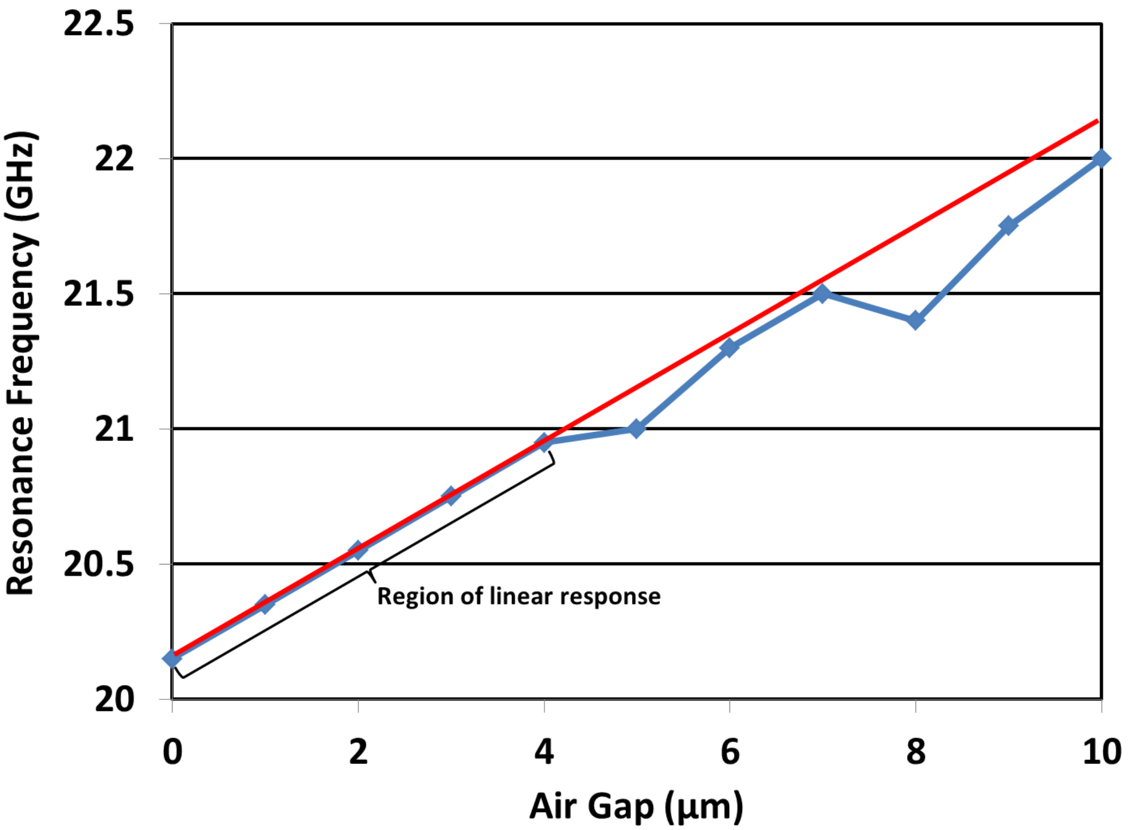

Figure 43 – Resonance frequency with respect to air gap for a scaled down version of the SRR based strain sensor. This sensor would operate in a bandwidth between 20 GHz and 21 GHz.

After scaling, the SRR still has decent performance, but the return loss of the device is much closer to -10 dB, or 10% reflection than the original implementation which operated in the GPS band. This is very near the acceptable limit for return loss of an antenna, so some slight redesign would be necessary to optimize the design to better match the input impedance to the standard 50 Ω coaxial line.

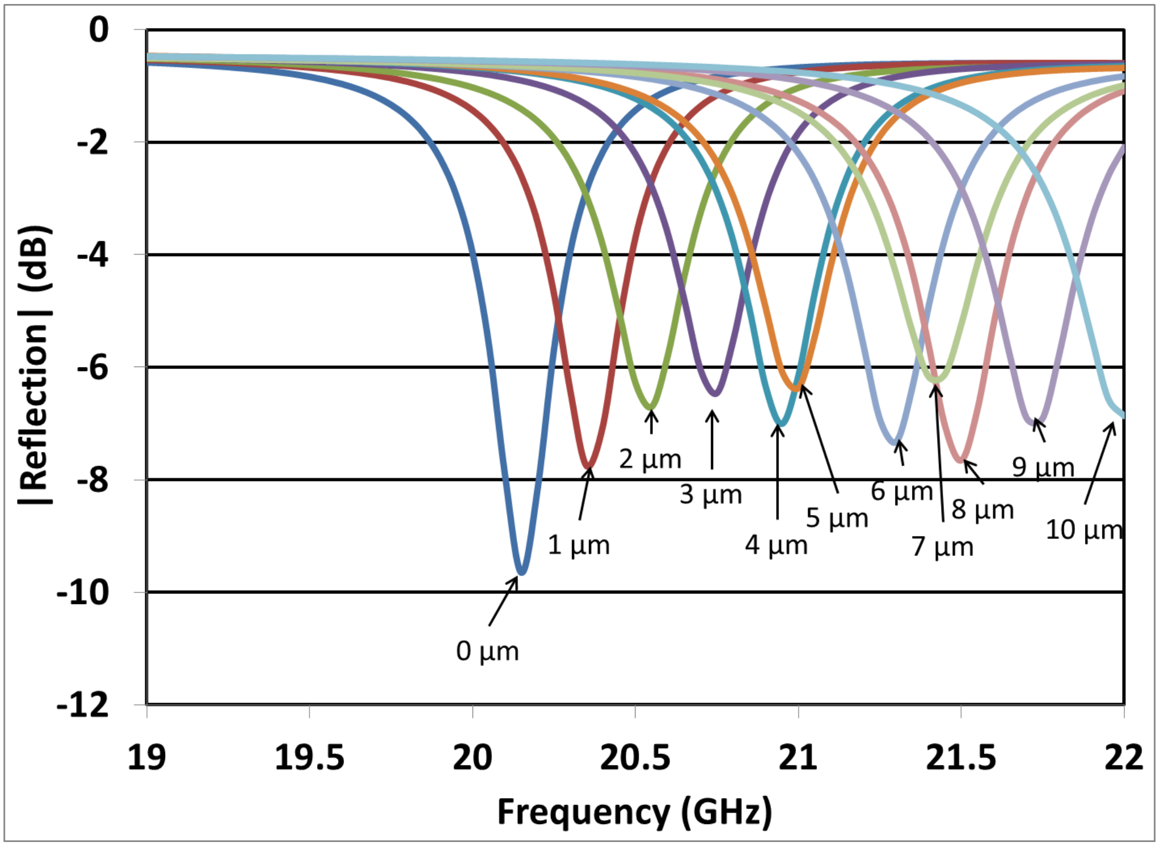

Figure 44 – Frequency response of the miniaturized aperture coupled SRR strain sensor

3.3 PCB Fabrication Techniques

After successfully simulating the antenna structure, it is necessary to fabricate the devices for measurement. Although there are several methods of fabricating printed circuit board (*PCB*) based devices, photolithography has the distinct advantage of having very high resolution, with resolution as good as 100 µm. An alternative method of PCB fabrication would be mechanically milling away excess conductor. This method, although extremely precise, has several downsides, such as the inability to cut square corners on the concave side of a trace and the extreme difficulty in ensuring that the conductor is completely milled away without removing any substrate material. An example of milling as opposed to etching a structure is provided in Figure 45, in which the defects remaining from the etching process are quite visible.

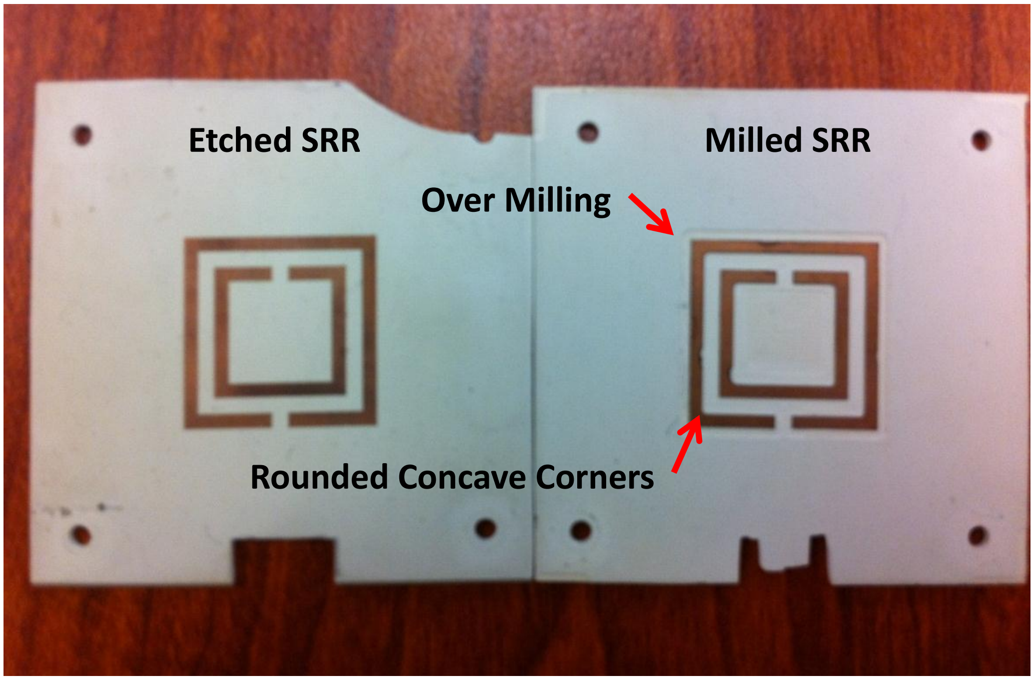

Figure 45 – Comparison between etched and milled SRR samples. The devices shown are identical except for the fabrication technique involved. The over milling and rounded corners are quite visible in the milled sample.

The antennas and sensors fabricated for this thesis were performed using negative photolithography. As shown in Figure 46, for the negative photolithography process, the regions of copper to be left as traces are exposed to UV light in order to leave the protective film of photoresist as protection from chemicals during etching. The entire procedure for fabricating the PCB's used to construct the SRR based strain sensor is outlined below.

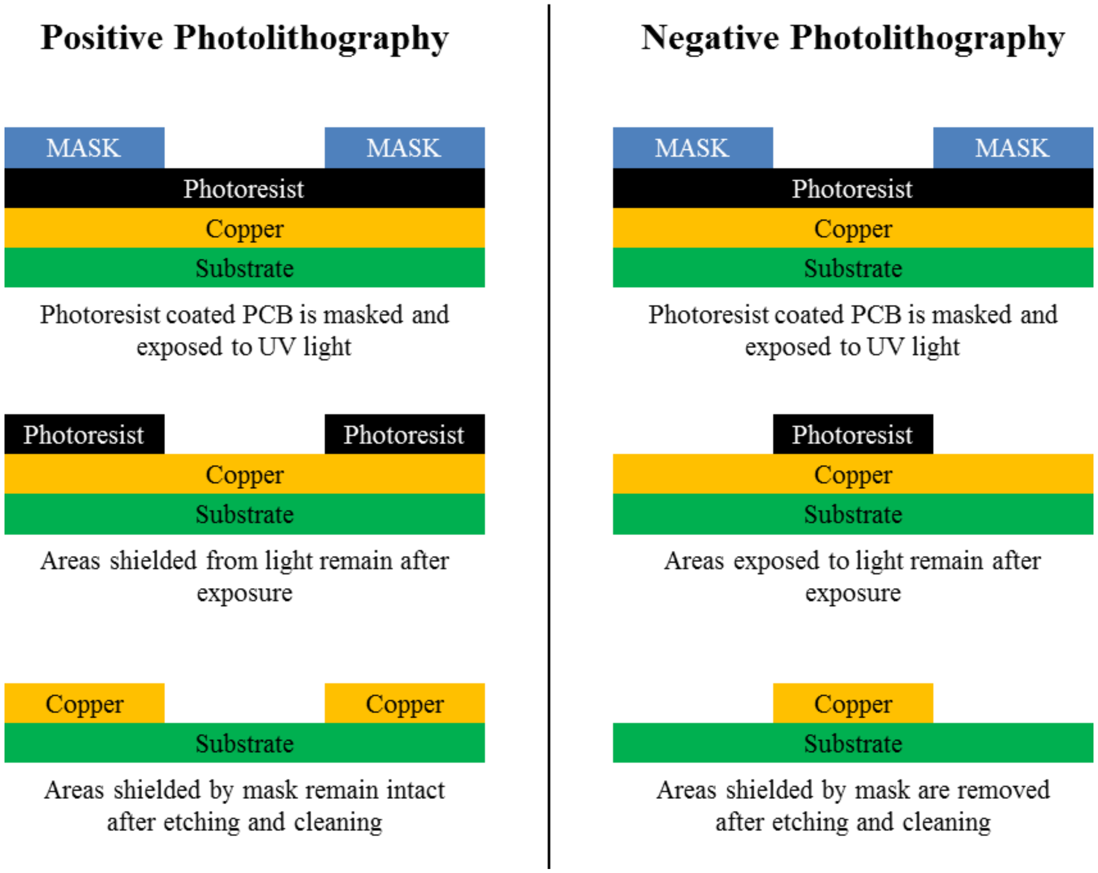

Figure 46 – Comparison between positive and negative photolithography. In essence for positive photolithography, the traces are dark, while for negative photolithography, the traces are clear and the field of the PCB is dark.

The process of photolithography first begins with preparing the board. The first step involved in this is cleaning. This is perhaps the most important step in the entire process as in order for the photoresist to adhere to the copper, it must have a clean surface to make contact. A dirty board will inevitably allow some resist to detach causing over-etching, ruining the board. After thoroughly scrubbing with soap, the board must be rinsed until water flows freely across the surface and then dried.

After cleaning, the board is ready for processing. All processing until the board is ready for etching must be performed in a dark room to prevent the resist from being exposed to UV light and partially developing he photoresist. In the dark room, the board is heated and given a coating of photoresist. The photoresist is applied such that there is a smooth, thin coat covering the entire surface of the copper to be patterned

Next, the board is covered with a photo-mask, printed on a transparent material with the areas to be removed blocked with ink. Once masked, the board is placed between two glass plates to ensure good contact between the mask and the board. A high wattage UV lamp is then used to expose the board for approximately 20 minutes. This is the step where the pattern is defined.

Negative photoresist is a liquid composed of short polymer chains. As the light strikes the resist coated surface, the chains align themselves and become much longer, resulting in an area which is more difficult for the etching solution to remove. This effect is invisible to the human eye, and the areas of ‘cured’ resist will only be visible after the uncured resist is washed away in the developing solution.

After exposure, the next step in processing is development. Developer is a solution in which the unexposed, uncured photoresist is soluble. As the board is allowed to soak in the developer, all areas which were obscured from the exposure lamp lose their coating of resist. This leaves behind only the bare copper in these regions which will be removed in the next step.

After development, the final step in board processing is etching. The etchant used is Ferric Chloride, an acid which is brown in color that removes the copper cladding from all unprotected areas of the board. The solution is heated in order to increase the etch rate and reduce over-etching of protected features.

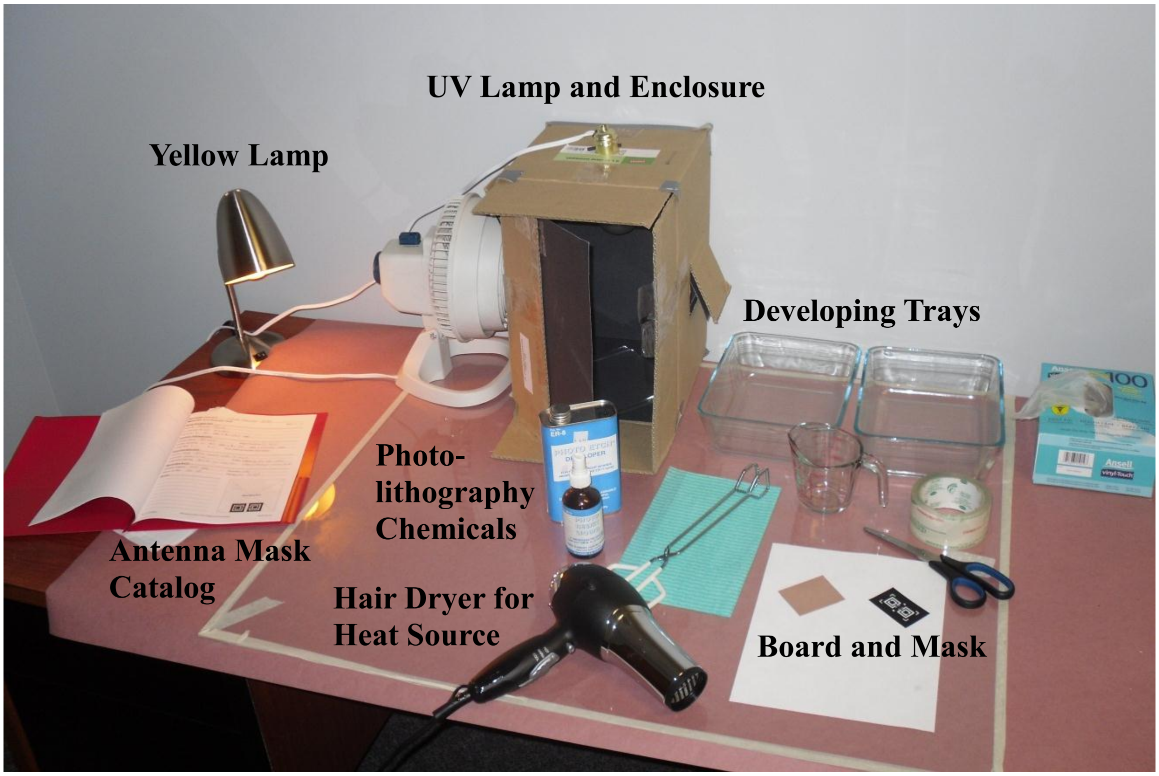

Figure 47 – Etching facility used for fabrication of SRR based antennas and strain sensor. A yellow lamp is required for the dark room to ensure no UV light is striking the unfinished circuit board.

Fast etching is crucial for a good result when using the Ferric Chloride solution as the resist is only covering the top layer of the copper. As the board is etched, it is possible for the acid to undercut and remove copper that would otherwise be protected, but given a quick enough etch, this will be minimal because the unprotected areas have much more surface area than the edges at risk of being undercut.

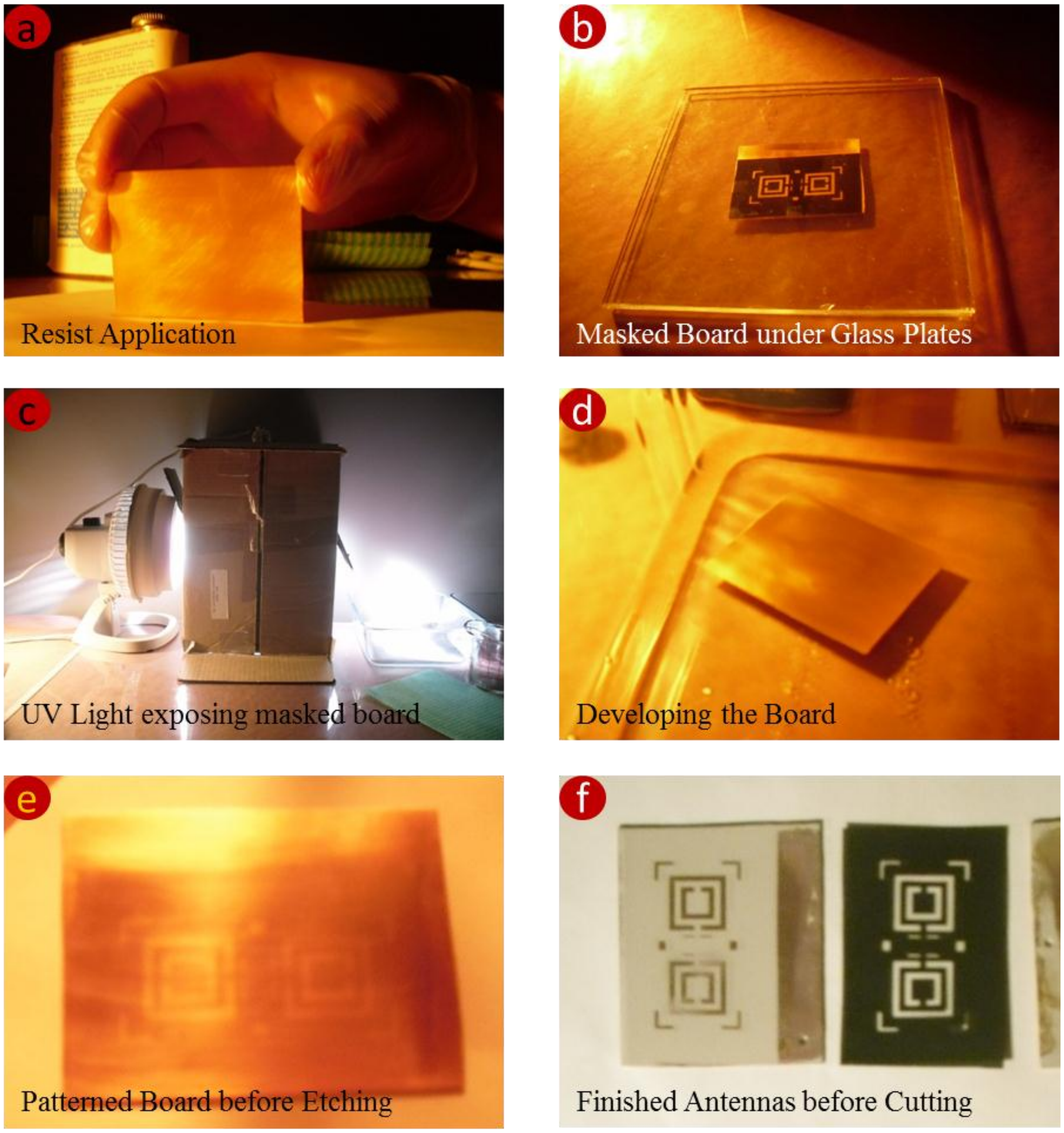

Figure 48 – Illustrated steps involved in photolithography process. The clean board is first given a coat of resist (a), masked and pressed between two glass plates (b), exposed to UV light for 20 minutes (c), developed in the developing solution (d), inspected for pattern clarity (e), and finally etched (f). After this process, the board is cut using a PCB saw to size and electrical connections are made.

IV. EXPERIMENTAL SETUP AND RESULTS

The experimental setup implemented for this concept consists of affixing both a traditional strain sensor and the new metamaterial strain sensor to a cantilever beam and loading the free end with weights of known mass. The individual components of the setup were the cantilever beam itself along with the loading masses, the resistive strain gauge and associated measurement equipment, the SRR based strain sensor and its associated measurement equipment, and the measurement equipment for determining the beam displacement.

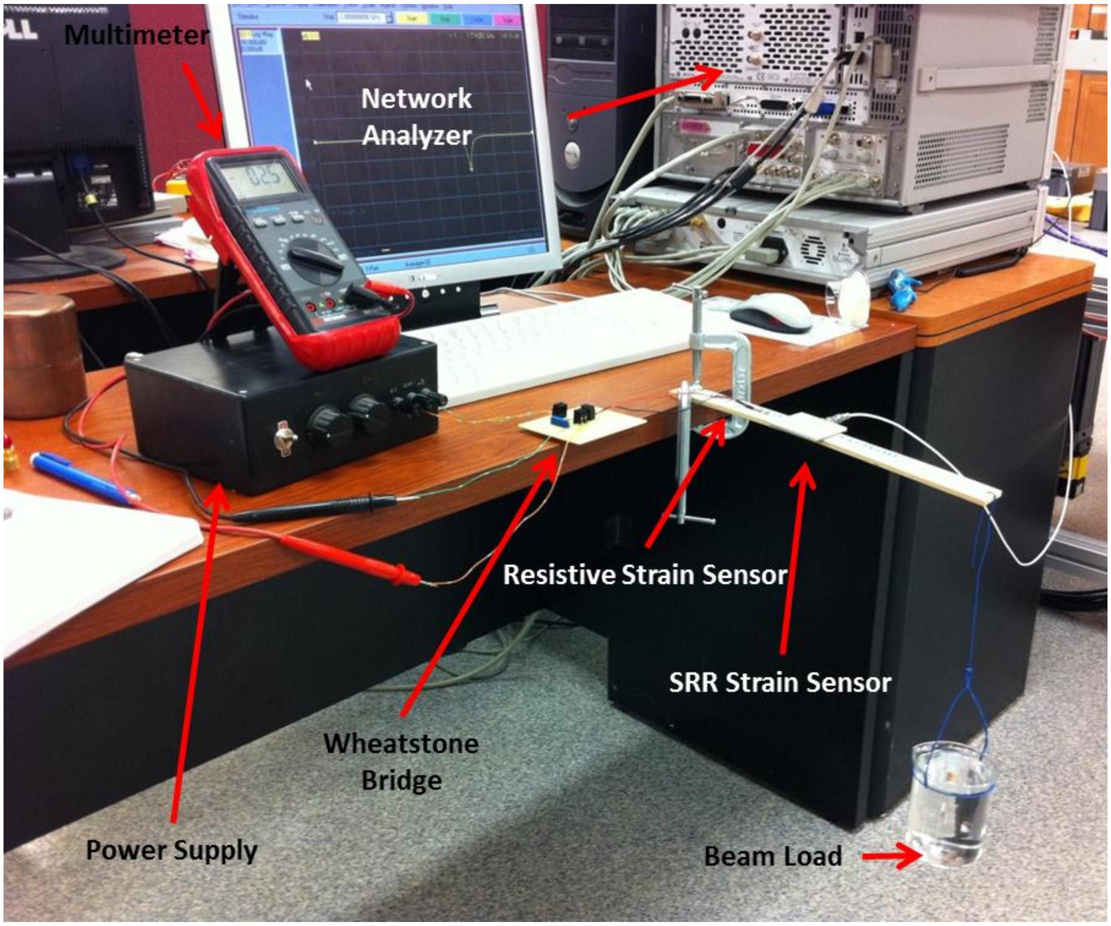

Figure 49 – Experimental setup for strain measurement. The SRR sensor is placed at 101.6 mm and the resistive strain sensor is placed at 76.2 mm. The Wheatstone bridge and multimeter are connected to the resistive sensor while the network analyzer is connected to the SRR strain sensor.

4.1 Cantilever Beam

The cantilever beam is comprised of a 30 cm section of a wooden ruler clamped to a desk. The beam is of small cross-section relative to length. The physical dimensions of the beam used for experimentation are 4.9 mm x 26.7 mm x 300.0 mm (h x w x l), as shown below. It is critical that the beam be of relatively small cross section as compared to the length of the beam for the cantilever beam approximation to be valid. In this case, the aspect ratio of the beam about the bending plane (thickness vs. length) is very large; 61.22, enough to allow the approximation to be used.

The beam is clamped to a desk using twin C-clamps in order to assure a truly rigid contact point from which to extend the beam. The beam is marked such that it may be affixed to the desk at a point such that there are 300 mm of beam extending beyond the edge of the desk.

Figure 50 – C clamps holding the beam to the desk. This ensures that the beam has a rigid anchor point allowing for the cantilever beam equations to be used.

Due to the method of mounting the strain sensors, discussed in detail below, only tensile strain may be measured with any single sensor for mechanical reasons. In order to measure compressive strain, the entire beam with sensors attached was inverted such that the sensors were now on the bottom face. By loading the beam in this manner, a compressive load is simulated. Due to the necessity of this configuration for the tensile and compressive experiments to be identical, all experimental results are the superposition of 2 data sets. The actual loading is performed by suspending beakers of known mass, partially filled with water, from the end of the beam using a thin wire. In order to accurately gauge the mass of the load, both the beaker with water and the wire were weighed together to obtain the appropriate mass.

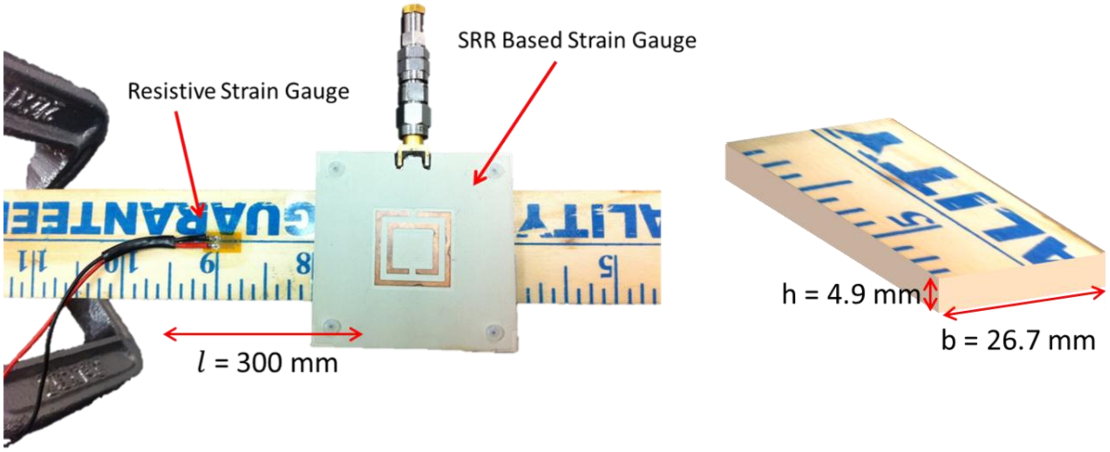

Figure 51 – Sensor placement on the cantilever beam. The beam itself is 300 mm in length with a cross sectional area of 130.8 mm^2.

4.2 Beam Deflection Measurement Setup

In order to verify the results obtained using the strain sensors theoretically, all properties of the beam must be known. The physical dimensions of the beam known, however the Young's modulus, necessary for calculating the expected deformation for a given load is still unknown due to the high variability between wood types. Wood is also somewhat inhomogeneous in comparison to materials such as steel and Plexiglas, however the small section of wood used in the beam for this experiment is free of any knots or other glaring inclusions, prompting the assumption of homogeneity.

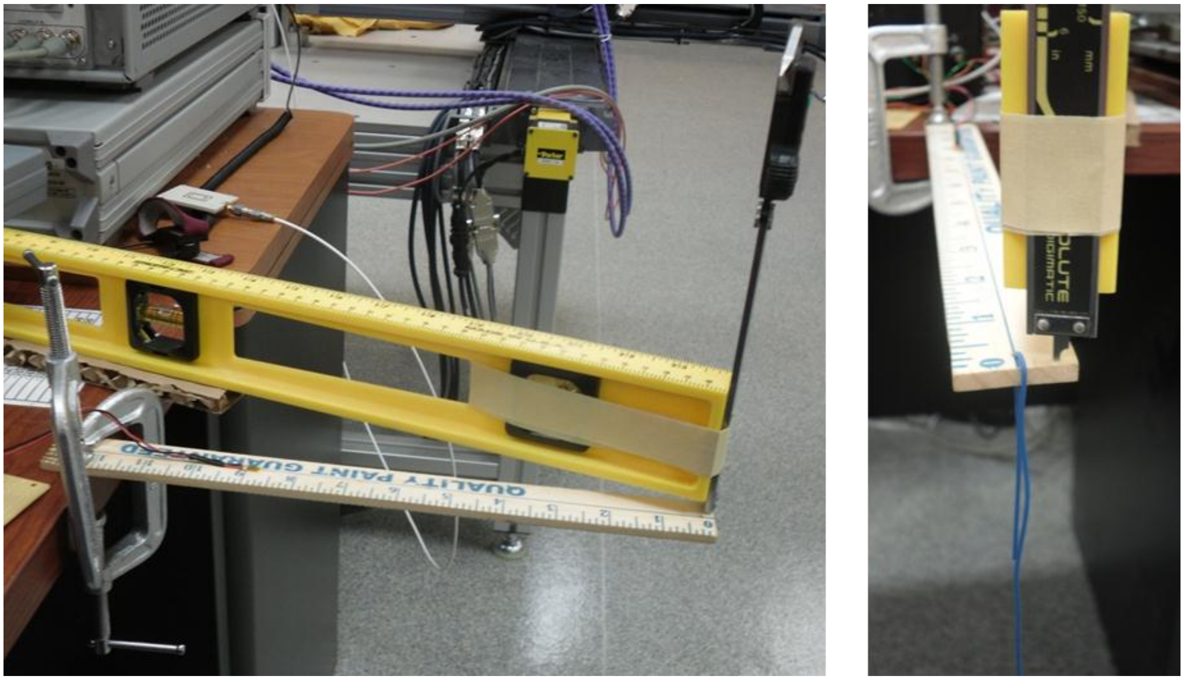

Figure 52 – Beam deflection measurement setup. The beam deflection is measured using a caliper zeroed to the rest position of the cantilever beam. As the beam is deflected, the caliper's depth probe is moved to the point where it makes minimal contact with the beam.

As mentioned in the background section on beam mechanics, the Young's modulus is found experimentally by determining deflection with respect to beam load. This measurement is performed using a digital caliper, affixed to a level to ensure a proper plane to measure from. The caliper is then zeroed such that the readout is at 0.000 mm under no beam load conditions. As each weight is applied to the beam, the caliper is adjusted such that the depth gauge of the caliper just touches the beam. This is assumed to be the distance of deformation of the beam. In reality, there is also horizontal deformation, however given the small amount of deflection this is assumed to be negligible. In order to assure that the displacement measurements are accurate, the displacement was measured over the course of several experimental runs.

4.3 Resistive strain sensor setup

The resistive strain sensor implemented in this experiment is a commercially available thin film strain gauge [2]. The gauge is manufactured using a polyimide sheet for a backing material. Polyimides have a very low Young's modulus, and hence, are extremely flexible, allowing for a more sensitive sensor. The metallic traces of this particular sensor are made from Constantan, a copper-nickel alloy known for having a very constant resistivity across a wide range of temperatures.

The resistive strain sensor is affixed to the cantilever using a cyanoacrylate adhesive as recommended by the manufacturer. This adhesive allows for the sensor to be affixed to the beam in such a manner that as the beam is deformed, the sensor will see the same deformation. Copper lead wires are run from the sensor back to a Wheatstone bridge circuit consisting of 2 identical resistors and a potentiometer to allow for the bridge to be fine-tuned for zero voltage drop across its output.

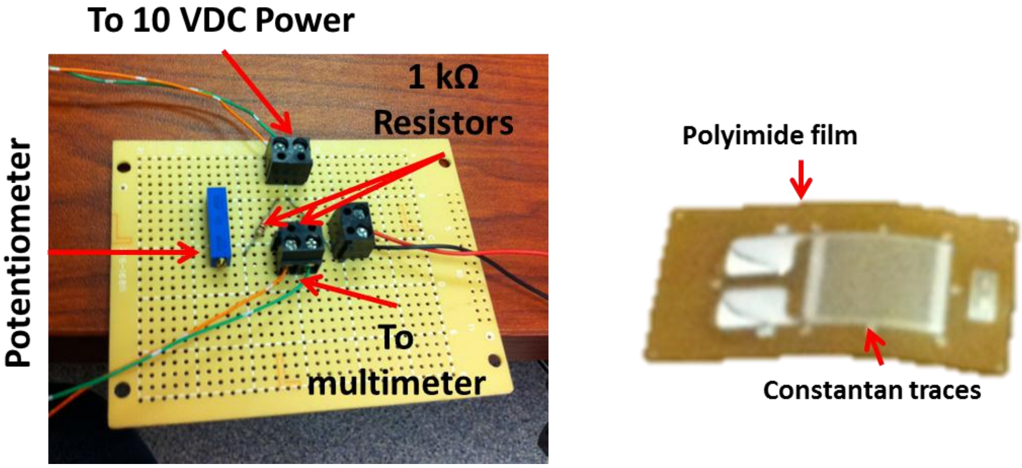

Figure 53 – Wheatstone bridge circuit implementation. The potentiometer is used to calibrate the bridge to a balanced state when there is no load at the end of the cantilever beam.

The Wheatstone bridge was powered using a custom built 10 VDC power supply in order to provide a large enough excitation voltage for the small changes in resistance of the sensor to produce a readable output without need for amplification.

4.4 SRR Strain Sensor setup

The SRR based strain sensor is affixed to the cantilever beam using a permanent double-sided tape which allows for a very firm grip, yet the ability to remove and relocate the sensor. Due to the fact that this sensor is based on a prototype antenna, affixing the sensor with cyanoacrylate glue such as with the resistive sensor is not possible. For the small amounts of strain being measured in this particular experiment, the sensor is assumed to be completely bonded to the beam. This is verified by the linear frequency response to applied strain observed in the previous chapter discussing the simulation and design of the strain sensor.

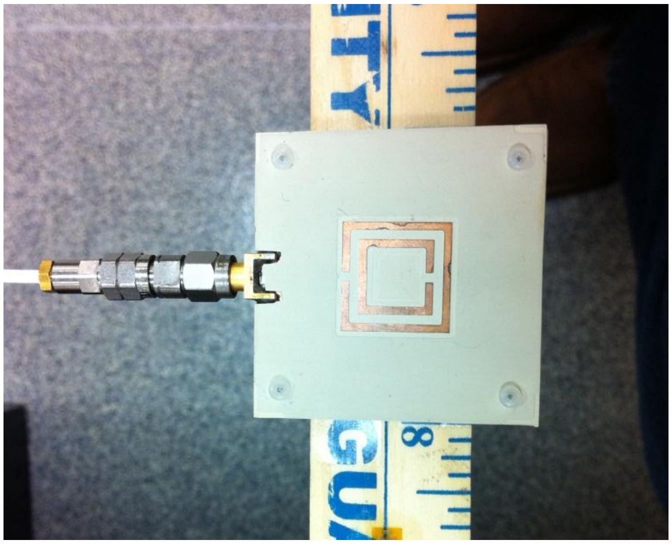

Figure 54 – SRR sensor affixed to the cantilever beam. The sensor as currently implemented is capable of measuring strain from either direction along the plane of the beam. Future variations could be made to eliminate the sensitivity of the sensor to one direction, giving the same net functionality as the resistive strain sensor.

Currently the strain sensor is capable of measuring strain in either direction along the plane in which it is placed. This capability can be altered to force the sensor to be sensitive only to strain along a single direction by adding additional mounting points along the edges of the sensor along the line in which strain is to be measured.

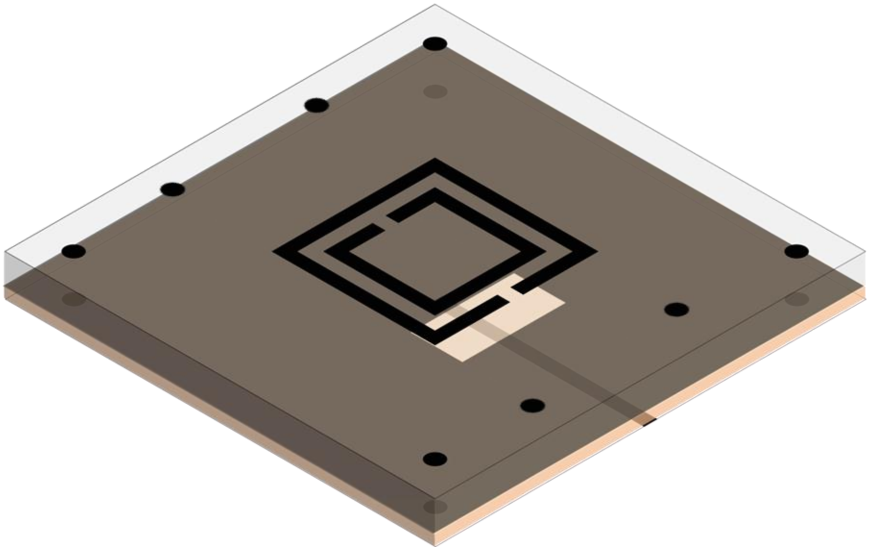

Figure 55 – By adding additional mounting points along the edges of the sensor parallel to the direction of desired sensitivity, the sensor can be made monodirectional; that is sensitive to strain only along one axis.

V EXPERIMENTAL RESULTS

In order to be viable, the SRR sensor must perform the same functions as the resistance based strain gauge. In addition to similar performance, both sensors should report values that corroborate the theoretical strain computed from on the end-loaded cantilever beam problem. The primary criteria that the SRR based antenna must meet in order to operate as a strain sensor are as follows:

- The antenna operating frequency should ideally vary linearly with strain, similarly to the resistive sensor experiencing a linear change in resistance.

- Regardless of the linearity of the SRR sensor response, the measured data should be unique for a given strain in order to differentiate between tensile and compressive strains.
- The measured strain should also be repeatable for the sensor to verify the precision of the device.

These criteria are tested individually for the SRR sensor and its performance is compared with the resistive strain gauge as well as theoretical calculations.

5.1 Frequency to Strain Relation

For a cantilever beam made of a material that is assumed to be linear, that is the Young's modulus is treated as a constant, causing strain to vary linearly with applied stress, the measured strain should vary linearly with the applied load. This means that a plot of measured resonance frequency of the SRR with respect to applied beam load should either be linear or approximated by a polynomial fit. Simulation results have shown that the expected behavior of the sensor is very close to a linear relation between air gap size and resonance frequency.

5.2 Behavior of Resonance: Tensile vs. Compressive Strain

Resistive strain sensors operate based on the physics of the resistance of a wire. As the wire is compressed, the overall length is reduced while cross section increases, causing a net drop in resistance, while the inverse is true for tension of the wire. This means that the resistive sensor is not only capable of determining the magnitude of the strain, but the type as well (compressive or tensile). In order for the SRR based sensor to match this behavior, the device's resonant frequency should shift in one direction from the rest frequency for compression, and shift in the opposite direction for tension. This behavior is shown below in Figure 56. As before, the variation in frequency is quite large for a given change in the beam's load, a desirable characteristic for precision.

More importantly, the SRR sensor's frequency response must be smooth and monotonic for implementation as a sensor. This means that there must be a unique resonance frequency for a given strain. For a parallel plate capacitive type sensor, this should be expected as the sensor capacitance is directly determined by the air gap between the plates.

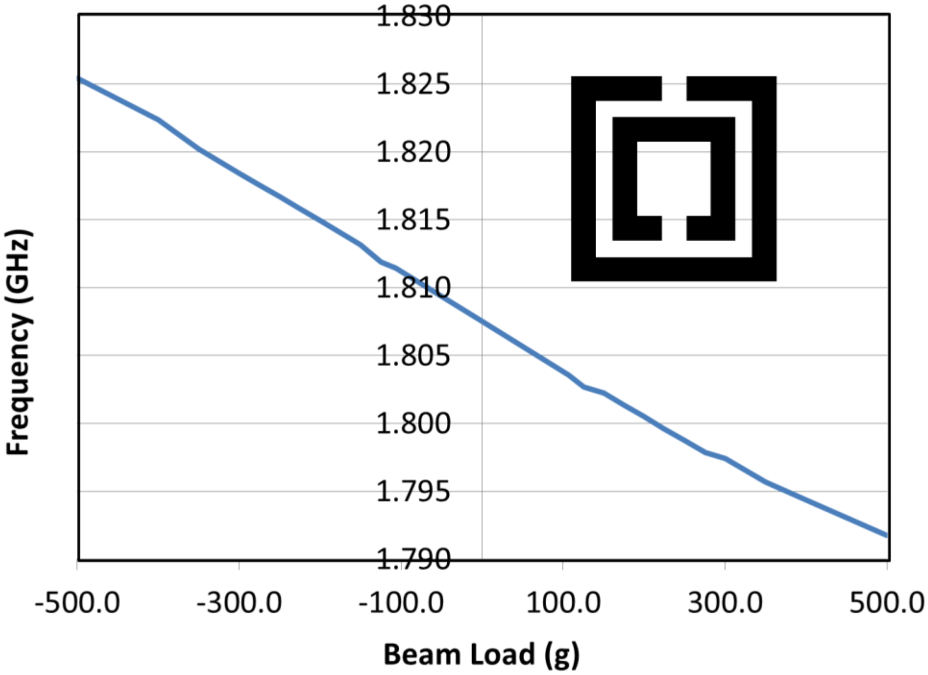

Figure 56 – Resonant frequency response of the SRR based strain sensor with respect to beam load. The sensor response is extremely linear, which will allow for a data inversion process similar to the traditional strain sensor.

5.3 Strain Quantification

Both the SRR strain gauge and the resistive strain gauge may be used to quantify strain, as is shown in the previous portions of this section. There is still the issue of converting the raw measurement data into a useful value, in this case strain. The manner of quantification of the resistive strain sensor, outlined in the introduction, involves the introduction of a gauge factor to scale the measured resistance to a strain. The SRR based strain gauge implements the same principle. The percent change in resonance frequency is scaled by a gauge factor to convert the measured resonance change into a measured strain. The gauge factor for any strain gauge is assumed to be a constant, and should allow for the correct inversion of strain regardless of the position of the sensor on the beam.

Resistive Strain Sensor

$$\Delta R = \frac{V(R_1 R + R_1 R_4 + R_2 R + R_2 R_4) - V_{src}(R_1 R_4 - R_2 R)}{V(R_1 + R_2) + V_{src} R_2}$$

$$\epsilon = \frac{\boldsymbol{\Delta R}}{\boldsymbol{R \cdot GF}}$$

$\epsilon \equiv strain$
$GF \equiv$ Gauge Factor
$R \equiv$ No Strain Sensor Resistance
$\Delta R \equiv$ Change in Resistance

SRR Based Strain Sensor

$$\Delta f = f - f_0$$

$$\epsilon = \frac{\mathbf{\Delta f}}{\boldsymbol{f_0 \cdot GF_{SRR}}}$$

$\epsilon \equiv$ Strain
$GF_{SRR} \equiv$ Gauge Factor of Sensor
$f_0 \equiv$ No Strain Resonance Frequency of Sensor
$f \equiv$ Resonance Frequency of Sensor with Strain

Figure 57 – Comparison of strain calculation techniques between the SRR based strain sensor and the resistive type strain sensor.

The gauge factor is defined in such a manner as to be nearly identical to that of the resistive strain sensor. This technique will be proven valid if the strain sensor is capable of correctly inverting the strain to a value matching the theoretically expected result at several points along the beam.

5.4 Measurement of Cantilever Beam Displacement

The displacement of the cantilever beam is a quantity that is necessary for the computation of the cantilever beam's Young's modulus. The measurement process, consisting of measuring the beam displacement as a function of beam load results in the determination of the Young's modulus. This quantity is plotted below, showing that the Young's modulus of the beam is indeed nearly constant, validating the assumption that the wooden cantilever beam used in the experiment is indeed a linear material. The data point for zero load is missing because the problem is undefined for the no load condition as there is no strain present on the beam, implying that no Young's modulus can be inverted.

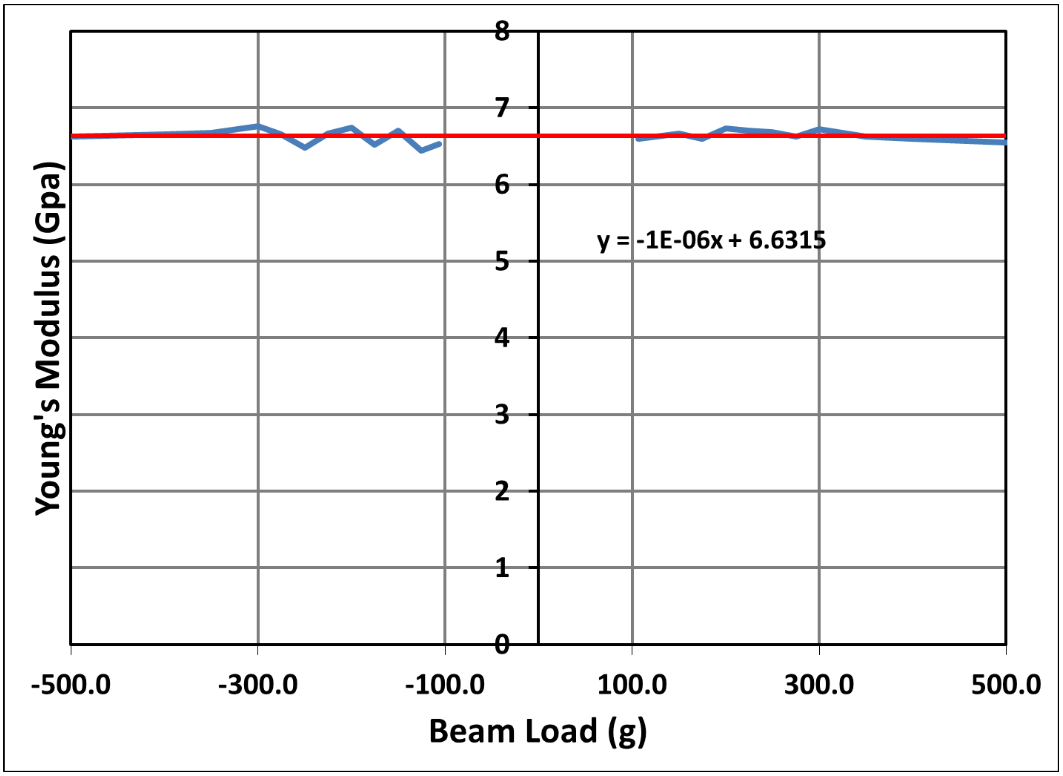

Figure 58 – Plot of the measured Young's modulus for the wooden cantilever beam as determined from experimental data. The Young's modulus is essentially a constant across all load conditions used during testing.

5.5 Comparison to Theoretical Calculation

Theoretically, the stress along the end loaded cantilever beam varies linearly with respect to distance for any given load which allows the beam material to show simple bending. This is verified experimentally using data taken from both the resistive strain sensor and the SRR based strain sensor at 101.6 mm from the base of the cantilever beam. Inverting the strain measured at this point will serve to show that the theoretical inversion is correct and that the calculated strain values correlate well with the expected results. Next, in order to verify that the SRR based strain sensor behaves in this manner, and is in fact operating as a strain gauge, the SRR sensor was placed in a second spot on the beam and the experiment of measuring the strain using a range of beam loads was repeated.

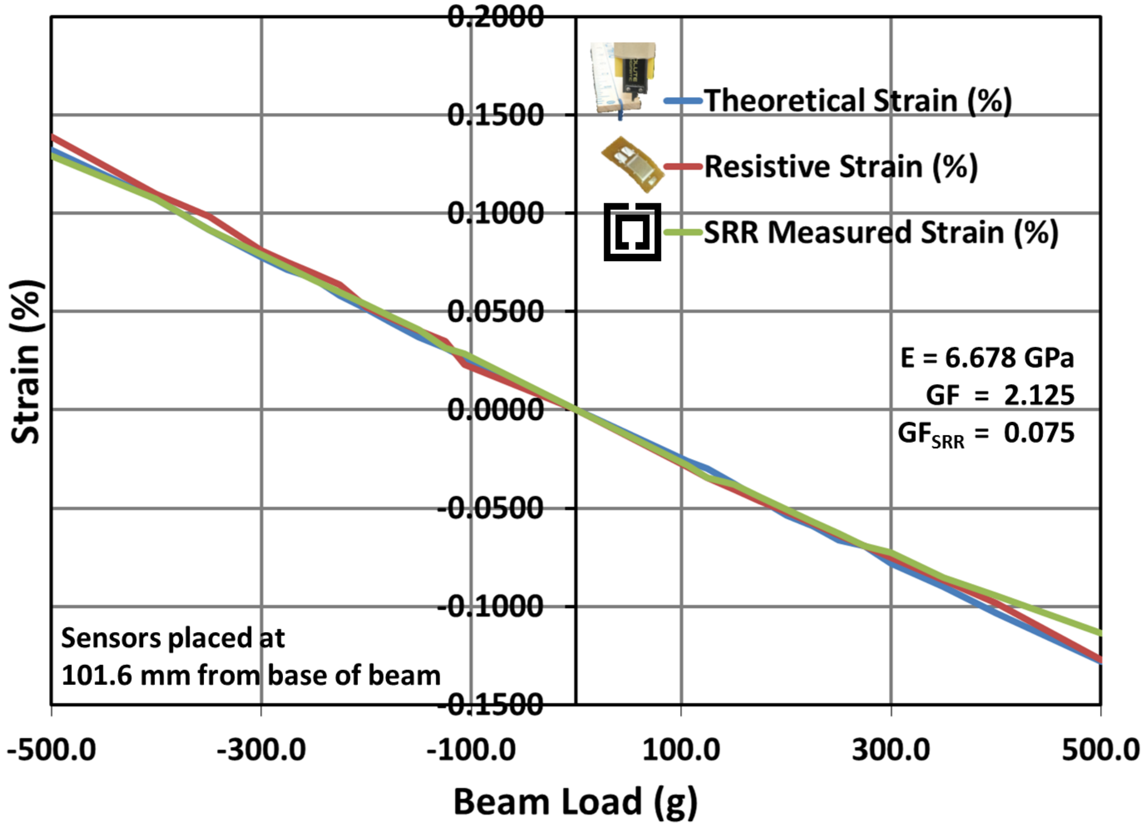

Figure 59 – Comparison between theoretical strain calculation, resistive strain measurement, and SRR based strain measurement all for sensors placed at 101.6 mm from the base of the beam. The results track extremely well for the single sensor location. This establishes the assumed

gauge factor for the SRR. This value will be used to invert data from a different location in order to verify that the gauge factor inversion technique is valid.

After establishing a gauge factor for the sensor, it is necessary to perform another strain measurement at a different beam location. For the second beam location, the sensor is connected at 177.8 mm rather than at 101.6 mm. As expected, the strain is much lower here as it should decrease linearly from the base to the loaded end of the beam. It is shown that the gauge factor defined earlier still holds when the sensor reading is taken from a different point on the beam, thus proving that the strain sensing mechanism is viable for applications where small strains are measured.

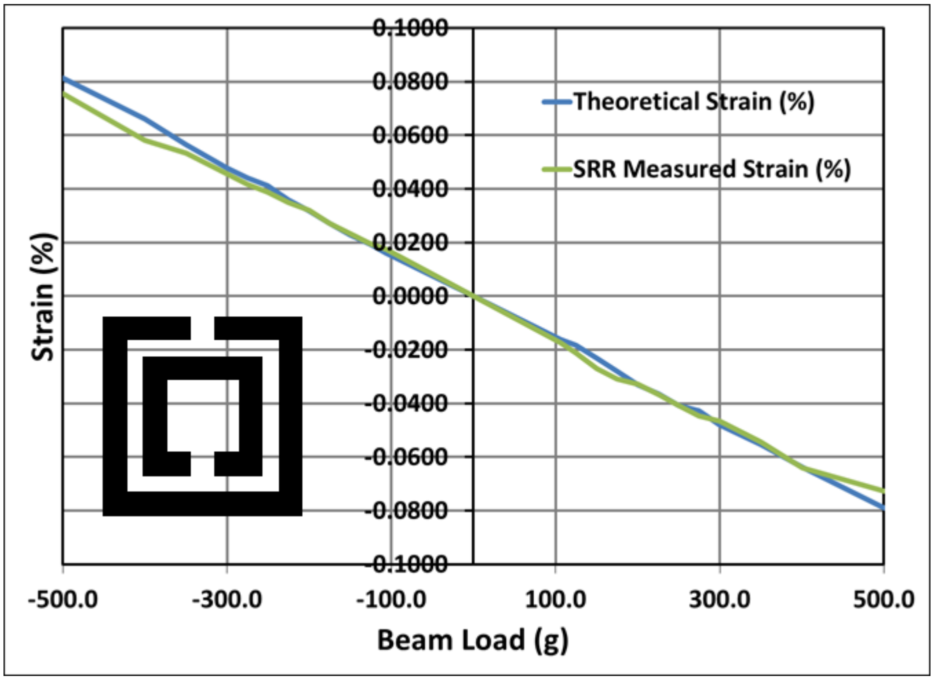

Figure 60 – Measured SRR strain sensor data at a distance of 177.8 mm from the base of the beam. This strain value is lower than that obtained from the point closer to the base of the beam as expected.

5.6 Measurement Repeatability

No sensor is useful if the measurement is not repeatable. Repeatability is established through several trials of the device using identical test conditions. As is shown below, the SRR based strain sensor exhibits behaviors that indicate it is quite capable of repeatable measurements, with an error of ± 0.03% strain over the three experimental iterations.

From a similar study performed on the resistive strain sensor, it is shown that the same linearity is present with the resistive strain sensor over all three trials. Also, the distance used for the resistive sensor study is different from that of the initial measurement. This sweep, using the same gauge factor as for the case of the sensor at 101.6 mm also inverts the strain properly, verifying the performance of the resistive strain sensor.

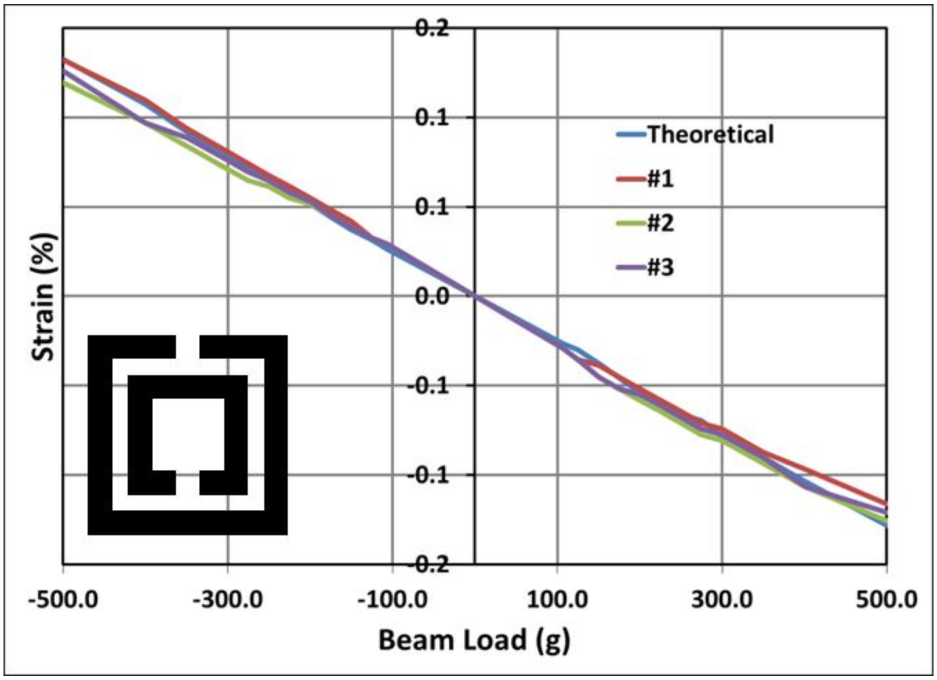

Figure 61 – Repeatability study performed using the SRR based strain sensor. The sensor is located at 101.6 mm and the results from 3 separate measurements are compared with the theoretically expected value for the given beam loads. This comparison shows that the SRR has very good linearity and is capable of measuring the strain accurately after several trials.

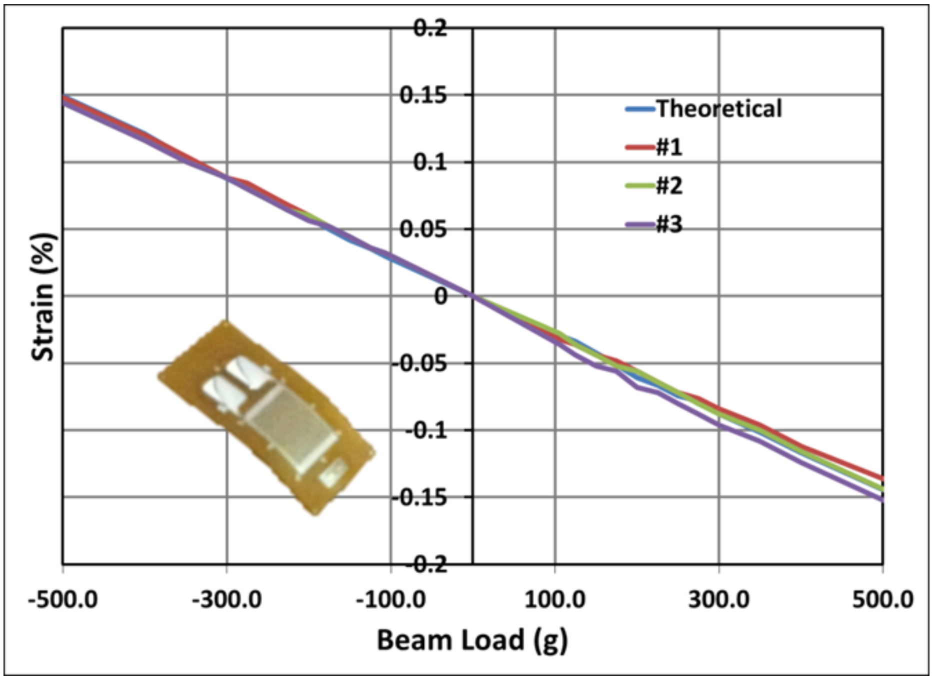

Figure 62 – Repeatability study for the resistive strain gauge. The strain was measured 3 times at 76.2 mm from the base of the cantilever beam for this set of data.

VI CONCLUSIONS AND FUTURE WORKS

The sensor used for experimentation in this thesis serves to provide proof of concept for the SRR based strain sensor, but it is still far from a viable competitor for a resistive strain gauge in commercial or industrial settings. The main issues with the sensor illustrated in this thesis are that it is both wired and quite large compared with current resistive sensor technology. However, these obstacles are not insurmountable. With proper design and optimization, the sensor may be altered in such a way as to realize a miniaturized wireless sensor using the change in dielectric loading as a novel approach for the sensing mechanism.

6.1 Miniaturization of the SRR Based Strain Sensor

In order to improve upon the design, the sensor can be scaled down to operate at a much higher frequency than originally designed. As shown in this thesis, the sensor could theoretically be scaled down to a size smaller than the resistive strain gauge while maintaining critical performance parameters. This alone is very promising, as it will allow for, at a minimum, a wired version of the strain sensor capable of exploiting the dependence on the SRR resonance to the properties of the substrate on which it is patterned, in effect, offering a microwave analog to the resistive strain sensor currently available. Future implementations of the sensor using substrates much thinner and with smaller traces should be capable of achieving the same level of performance in a wired scenario as the reflection minimum is the physically measured quantity.

6.2 Wireless Implementation of the SRR Based Strain Sensor

To devise a wireless strain sensor, the SRR must be situated in such a way that it can affect the resonant frequency of an antenna. This can possibly be accomplished through the direct use of the SRR as a radiating element as in [22], or through the implementation of a planar sample which will use the resonance to absorb incident microwave energy of a certain frequency as described by Melik, *et al* [9], [12]-[14], creating a bandstop filter whose center frequency is determined by strain. Both of these approaches can be produced using current fabrication technology with cheap plastic or composite substrates such as capton or FR4.

REFERENCES

[1] Budynas, Richard, and Nisbett, J. K., "Shigley's Mechanical Engineering Design, 8th ed.," McGraw Hill, 2006, Print.

[2] Vishay Precision, "General Purpose Strain Gages – Linear Pattern," available online at http://www.vishaypg.com/docs/11194/125ad.pdf, Doc. No. 11194, Jan 2010

[3] Vishay Precision "Gage Series – Stress Analysis Gages," available online at http://www.vishaypg.com/docs/11506/gageser.pdf, Doc. No. 11506, Feb 2010

[4] Vishay Precision, "Surface Preparation for Strain Gage Bonding," available online at http://www.vishaypg.com/docs/11129/11129_b1.pdf, Doc. No. 11129, Aug 2010

[5] Varadan, V.K., "Microsensors, MEMS, and Smart Devices," ISBN 047186109, Wiley, 2001, Print.

[6] Kon, S., Oldham, K., "Piezoresistive and Piezoelectric MEMS Strain Sensors for Vibration Detection," Sensors and Smart Structures Technologies for Civil, Mechanical, and Aerospace Systems, 2007

[7] Jung, S., Ji, T., Xie, J., Varadan, V.K., IEEE Proc, "Flexible Strain Sensors Based On Pentacene-Carbon Nanotube Composite Thin Films," Aug 2007

[8] Varadan, V.K., Teo, P.T., Jose, K.A., Varadan, V.V. "Design and Development of a Smart Wireless System for Passive Temperature Sensors," IOP Science, Smart Mater. Struct. 9, 2000, 379-388.

[9] Jung, S., Ji, T., Varadan, V.K., "Flexible Strain Sensors Based on Pentacene-Carbon Nanotube Composite Thin Films," IEEE Proc. 7th Internat. Conf. Nanotech., Aug. 2007

[10] Melik, R., Demir, H.V., "Flexible metamaterials for wireless strain sensing," Appl. Phys Lett. 95, Nov 2009

[11] Vardan, V.V., Varadan, V.K., et al., "Wireless IDT Strain Microsensor," IOP Science, Smart Mater. Struct. 8, 1997, 745-751

[12] Melik, R., Demir, H.V., ",Metamaterial based telemetric strain sensing in different materials" Optics Express, vol. 18, No. 5, Mar 2010

[13] Melik R., Demir, H.V., "Nested Metamaterials for Wireless Strain Sensing," IEEE Jour. Quant. Elect., vol. 16, No. 2, Mar/Apr 2010

[14] MelikR., Demir, H.V., "Metamaterial-based wireless strain sensors," Appl. Phys. Lett. 95, Jul 2009

[15] Varadan, V.V., Ji, L., "Does a Negative Refractive Index always result in Negative Refraction? – Effect of Loss," MTT '09. IEEE MTT-S International, June 2009

[16] Wright, D.W., Cobbold, S.C., “The Characteristics and Applications of Metamaterials,” Royal Science of Medicine Press, Ultrasound 2009; 17: 68-73

[17] Ambati, M., Fang, N., Sun, C., “Surface resonant states and superlensing in acoustic metamaterials,” Phys. Rev. B, 75, 195447, 2007

[18] Pendry, J. B., “Negative refraction,” Contemp. Phys. 45, 191-202 2004.

[19] Veselago, V.G., “The Electrodynamics of Substances with Simultaneously Negative Values of ε and μ,” Sov. Phys. Usp. 10, 509 1968

[20] Pendry, J.B., Smith, D.R., “The Quest for the Superlens,” Sci. American, vol. 294, No. 7, pg. 42-9, 2006

[21] Kim, I.K., Varadan, V.V., “Electrically Small, Millimeter Wave Dual Band Meta-Resonator Antennas,” IEEE Trans Ant. Prop., vol. 58, No. 11, Nov 2010

[22] Varadan, V.V., Kim, I.K., Buscher, M.B., “Electrically Small Isotropic Antenna using Small Dipole and Split Ring Resonator,” to be published

[23] Bilotti, F., et al, “Design of Spiral and Multiple Split-Ring Resonators for the Realization of Miniaturized Metamaterial Samples,” IEEE Micro. Theory Techniques, vol. 55, No. 12, Dec 2007

[24] Smith, D.R., Kroll, V.N., “Negative Refractive Index in Left-Handed Materials,” Appl. Phys. Lett., vol. 17, No. 14, Oct 2000

[25] Sheng, Z., Varadan, V.V., “Tuning the effective properties of metamaterials by changing the substrate properties,” Jour. Appl. Phys. 101, Jan 2007.

[26] Varadan, V.V., Ji, L., “Temperature Dependence of Resonances in Metamaterials,” IEEE Trans Micro. Theory and Technique, vol. 58, No. 10, Oct 2010

[27] Kim, I.K., Varadan, V.V., “Effect of Capacitive Coupling between Split-Ring Resonators,” IEEE 2008

[28] Kim, I.K., Varadan, V.V., “LTCC Metamaterial Substrates for Millimeter-Wave Applications,” IEEE Reg. 5, Apr 2007

[29] Kim, I.K., Varadan, V.V., “Electric and magnetic resonances in symmetric pairs of split ring resonators,” Jour. Appl. Phys. 106, Oct 2009.

[30] Varadan, V.V., Sheng, Z., “Direct Comparison of the Magnitude and Phase of Measured S-parameters of Metamaterials with Finite Element Simulation,” IEEE 2006

[31] Dutta, Atanu M.S, “Design and fabrication of split ring resonator antennas with aperture coupled feeding mechanism,” University of Arkansas, Dissertation, MAI 49/03, Jun 2011

[32] Aydin, K., Bilotti, F., Ozbay, E., "Split-Ring-Resonator-Coupled Enhanced Transmission through a Single Subwavelength Aperture," Phys Rev. Lett., 102, 013904, 2009

[33] Ansoft Corp., "User's Guide – High Frequency Structure Simulator," Rev. 1.0, Jun 2005

[34] Pozar, D.M., "Microwave Engineering, 2nd ed.," ISBN 0471170968, Wiley, 1997

[35] Occup. Safety and Health Admin., "Electromagnetic Radiation: Field Memo," available online at: http://www.osha.gov/SLTC/radiofrequencyradiation/electromagnetic_fieldmemo/electromagnetic.html#section_6, May 1990

[36] Wheeler, H.A., "The Radiansphere around a Small Antenna," Proc. of IRE, 1959

[37] Pozar., D.M., Kaufman, B., "Comparison of three methods for the measurement of printed antenna efficiency," IEEE Trans. Ant. and Prop., vol. 36, No. 1, Jan 1988

[38] Newman, E.H., Bohly, P., Walter, C. "Two methods for the measurement of antenna efficiency," IEEE Trans. Ant. and Prop., vol. AP-23, No. 4, Jul 1975

[39] McKinzie, W.E., "A Modified Wheeler Cap Method for Measuring Antenna Efficiency," IEEE 1997

[40] Balanis, C.A., "Antenna Theory: Analysis and Design, 3rd Edition," Wiley, ISBN 047166782, 2005.